JOURNAL OF MATERIALS RESEARCH AND TECHNOLOGY 2023;24:1949–1972

Available online at www.sciencedirect.com

jmr&t Journal of Materials Research and Technology

journal homepage: www.elsevier.com/locate/jmrt

Original Article

Friction stir processing of hybridized AZ31B magnesium alloy-based composites by adding CeO_2 and ZrO_2powders: mechanical, wear, and corrosion behaviors

Shoufa Liu [a], *Moslem Paidar* [b,*], *Olatunji Oladimeji Ojo* [c], *Michaela Šlapáková Poková* [d], *Sadok Mehrez* [e,f], *Azlan Mohd Zain* [g], *Qiaorong Zhao* [a], *Jinpeng Wang* [h]

[a] *School of Mechanical Engineering, Xijing University, Xi'an, Shaanxi 710123, China*
[b] *Department of Materials Engineering, South Tehran Branch, Islamic Azad University, Tehran 1459853849, Iran*
[c] *Department of Industrial and Production Engineering, The Federal University of Technology Akure, Nigeria*
[d] *Faculty of Mathematics and Physics, Charles University, Ke Karlovu 5, 121 16 Prague, Czech Republic*
[e] *Department of Mechanical Engineering, College of Engineering at Al Kharj, Prince Sattam Bin Abdulaziz University, 11942, Saudi Arabia*
[f] *Department of Mechanical Engineering, University of Tunis El Manar, ENIT, BP 37, Le Belvédère, 1002, Tunis, Tunisia*
[g] *Faculty of Computing, Universiti Teknologi Malaysia, Skudai, Johor 81310, Malaysia*
[h] *College of Mechanical Engineering, Xi'an Aeronautical Institute, Xi'an, Shaanxi 710077, China*

ARTICLE INFO

Article history:
Received 13 January 2023
Accepted 5 March 2023
Available online 10 March 2023

Keywords:
Friction stir processing
AZ31B magnesium
Cerium oxide
Zirconium dioxide
Mechanical properties
Wear

ABSTRACT

To improve the properties of AZ31B Mg alloy and for the first time, the rare earth cerium oxide (CeO_2) and zirconium dioxide (ZrO_2) were combined for synergistic benefits and introduced into the structural AZ31B magnesium alloy through the solid-state friction stir processing procedure to form the hybridized AZ31B Mg/ZrO_2+CeO_2 composites under variable levels of the tool's rotational speed up to 1200 rpm. The macro-/microstructure, hardness, shear punching strength, tensile strength, corrosion behaviours, and tribological characteristics such as weight/wear loss, wear rate, coefficient of friction, worn surfaces, and debris of the AZ31B Mg/ZrO_2+CeO_2 hybrid composites were investigated and compared. The results indicated that void, tunnel defect, and ZrO_2+CeO_2 agglomeration could not be prevented at low speed (800 rpm) while defect-free composites were obtained at high speed (1200 rpm). Grain refinement from 7.39 μm to 3.38 μm and the ZrO_2+CeO_2 fragmentation (4.52–2.49 μm) ensued after a rise in the tool's rotational speed owing to higher plastic straining, dynamic recrystallization, and ZrO_2+CeO_2 particle-aided pinning effects. Improvements in hardness (99–135 HV), shear punching strength (121–237 MPa), tensile strength (172–228 MPa) and wear properties of the composite were attained due to the defect elimination, inherent finer Mg grains, and the uniformly dispersed ZrO_2+CeO_2 particles. These attributes also enhanced the corrosion resistance of the AZ31B Mg/

* Corresponding author.
E-mail address: m.paidar@srbiau.ac.ir (M. Paidar).
https://doi.org/10.1016/j.jmrt.2023.03.028

ZrO_2+CeO_2 composite at the elevated rotating speed of the tool. The combination of the CeO_2 and ZrO_2 particles is an effective particle-blend for improving the properties of Mg alloy to expand its application scope.

1. Introduction

Magnesium alloy seats at the pinnacle of lightweight metallic materials with a density about 35% lower than Al alloy [1]. This unique attribute has made Mg alloys the best option for weight-saving structural applications in transportation and other industries like automotive, defence, aviation, and aerospace industries. However, the wide application of magnesium (Mg) alloys has been limited on account of their poor corrosion resistance, undesirable tribological characteristics, and inadequate mechanical properties such as poor formability, and low elastic modulus [1,2]. The intrinsic dense hexagonal close-packed structure of Mg has been acknowledged as a factor accountable for its poor formability and low ultimate tensile strength [3]. The development of Mg metal matrix composites via the use of stiffer and harder reinforcements has evolved as a notable approach for circumventing the shortcomings of Mg alloys [2]. Casting (stir and squeeze) [4], semi-powder metallurgy [5], molten metal infiltration [6,7], and friction stir processing (FSP) have been utilized in developing particle-reinforced Mg composites. Wettability issues, blow holes/porosity, and poor biological and anticorrosion performances are the common inadequacies of the traditional methods of producing Mg metal matrix composites [8,9]. These challenges can be surmounted via the usage of the solid-state-friction stir processing (FSP) method as it employs severe plastic deformation with coupled thermomechanical effect to establish recrystallized grains and desired microstructural changes. Thus, the FSP method introduces the combined effect of grain refinement, textural modification, and particle-induced dislocation strengthening into Mg-based composites to improve their properties.

Low processing cost, easy handling, and resistance to atmospheric corrosion are also some of the benefits of the FSP technique in developing Mg-based composite [3]. Reinforcements such as borides, carbides [10], oxides, nitrides, graphene [11], carbon nanotubes [12], and Ti [13] have been utilized in the production of Mg-based metal matrix composites in literature. The nature or type of reinforcements has been shown to have a significant impact on the tribological, corrosion, and mechanical performances of Mg metal matrix composites. The SiO_2 particles easily reacted with the AZ31 Mg to form the Mg_2Si phase during the FSP process of the composite [2]. Vedabouriswaran and Aravindan [14] investigated the reinforcement of RZ 5 Mg alloy with different particles such as B_4C, multi-walled carbon nanotubes (MWCNTs), and ZrO_2. The ultimate tensile strengths of the RZ 5/MWCNT, RZ 5/ZrO_2+Al_2O_3, and RZ 5/B_4C composites were 250 MPa, 260 MPa, and 320 MPa respectively. The Hall-Petch strengthening mechanism was reported as the governing mechanism for the enhancement of the strength of the RZ 5 Mg-based composite. Liu et al. [15] studied the reinforcement of AZ31 Mg alloy with Al, Al–Si, and Al–SiC particulates. The α-Mg and β-$Al_{12}Mg_{17}$ intermetallic phases were present in both the base alloy as well as the developed composite but the mean sizes and distributions of these phases decreased after the FSP process. It was reported that the highest corrosion potential (−1.19 V) and lowest corrosion current density (4.37×10^{-5} A) were found in the AZ31/Al–SiC and AZ31/Al–Si composites respectively.

Cerium oxide (CeO_2) and zirconium dioxide (ZrO_2) are important oxides with unique attributes that can be combined to attain synergetic benefits in hybridized Mg-based composite. CeO_2 is an attractive rare earth oxide with positive electrochemical action [16,17] or electrochemical stability [18], excellent ultraviolet absorption properties [19], thermal stability, high hardness, and excellent wear resistance [20]. Meanwhile, the crystalline particles of ZrO_2 are very stable and the FSP processing of the Mg/ZrO_2 composites has led to the formation of no chemical reaction between Mg and ZrO_2 particles in the studies of Chang et al. [2]. The use of these important oxides in combined form for the reinforcement of Mg alloys or the formation of a hybrid Mg-based composite has not received sufficient attention in the literature. However, these oxides have been individually employed as reinforcement particulates in literature for the development of Al and Mg-based composites. Mazaheri et al. [21] investigated the tribological characteristics of the FSP'ed AZ31/ZrO_2 surface nanocomposite. The wear property (rate) of the processed AZ31/ZrO_2 composite was reduced by about 40% as related to the base AZ31 alloy. The addition of ZrO_2 particles to AZ31 Mg alloy was reported to have enhanced the severe plastic deformation and the strain rate of the materials during the friction stir processing [22]. According to Sathish et al. [23], the packing of ZrO_2 particles within the AA6056 matrix improved the breaking strength of the developed composite while all the properties of the AA6061/ZrO_2 composites were enhanced with the exclusion of ductility in the studies of Kumar et al. [24]. Similarly, the introduction of 2 wt % CeO_2 into WC particles was reported to have reduced the aspect ratio of the WC particles and minimized the free energy between the matrix and WC particles in the study of Shu et al. [25]. The CeO_2 particles improved the properties of the AA6061/CeO_2 composite [26] and also caused the refinement of α-Al grain, and the improvement in hardness (124 HV), yield strength (87 MPa), and wear behavior of the AA2219/CeO_2 composite [27].

The solid lubricating attribute of rare earth CeO_2 oxide [28] and the nonreactive/stable property of ZrO_2 [2] are considered desirable properties that can be combined for the development of Mg/CeO_2 + ZrO_2 hybrid composite. To the best of our

Table 1 – Elemental compositions of the AZ31B magnesium alloy.

Material	Mg	Zn	Al	Mn	Si	Fe
AZ31B	Rest	1.11	3.01	0.61	0.12	0.005

Table 2 – Mechanical properties of AZ31B magnesium alloy.

Material	Tensile strength (MPa)	Yield strength (MPa)	Elongation (%)	Hardness (HV)
AZ31B	241	153	13	72

understanding, the development of Mg/CeO_2 + ZrO_2 hybrid composite through FSP processing is yet to be given attention in the literature. However, some other hybrid Mg-based composites are available in the literature. Hybridization of reinforcements has been revealed to improve the friction coefficient and wear resistance of the AZ31/ZrO_2/B_4C composite [29]. The improved hardness (19.7%) and compressive strength (77.5%) relative to the base metal were attained in the friction stir processed AZ31/MWCNTS/Graphene hybrid composite at a processing speed of 1400 rpm [11]. Grain refinement-assisted strengthening was acknowledged as the dominant strengthening mechanism in the hybrid composite. The friction stir processed Mg/$ZrSiO_4$/Al_2O_3 hybrid composite was developed by Sharifitabar et al. [30] via a multi-pass FSP processing route. This was reported that the multi-passes did not have a weighty impact on the properties of the Mg/Al_2O_3/$ZrSiO_4$ hybrid composite but the thermal cycle was affected during the FSP process. The multi-pass processing of AZ31 Mg led to the diffusion and homogenized dispersion of the β-$Al_{12}Mg_{17}$ precipitates at the stir zone of the alloy [31].

Based on the paucity of studies on the hybridized Mg/ZrO_2+CeO_2 composites in literature, this study is thus initiated. The synergetic properties of the rare earth CeO2 and the stable ZrO_2 are introduced into the AZ31B magnesium alloy to form the AZ31B Mg/ZrO_2+CeO_2 hybrid composite through the usage of the FSP technique under a variable tool rotational speed. The microstructures, mechanical (hardness, shearing, and ultimate tensile strength), corrosion, and tribological properties of the FSP'ed AZ31B Mg/ZrO_2+CeO_2 hybrid composites were examined in detail.

2. Materials and experimental procedures

Metal sheets of AZ31B magnesium alloy (5 mm thick) and the CeO_2 and ZrO_2 powders were the materials utilized in this study. A quantometer analysis was employed to obtain the elemental compositions of the AZ31B Mg alloy (see Table 1) while the tensile and hardness properties of the as-received Mg alloy are shown in Table 2. The Field-Emission Scanning Electron Micrographs (FE-SEM) as well as the X-ray diffraction (XRD) outcomes of the ZrO_2 and CeO_2 powders are presented in Fig. 1a–d. The mean particle sizes of the zirconium dioxide (ZrO_2) and cerium oxide (CeO_2) particulates are 8 and 12 μm respectively.

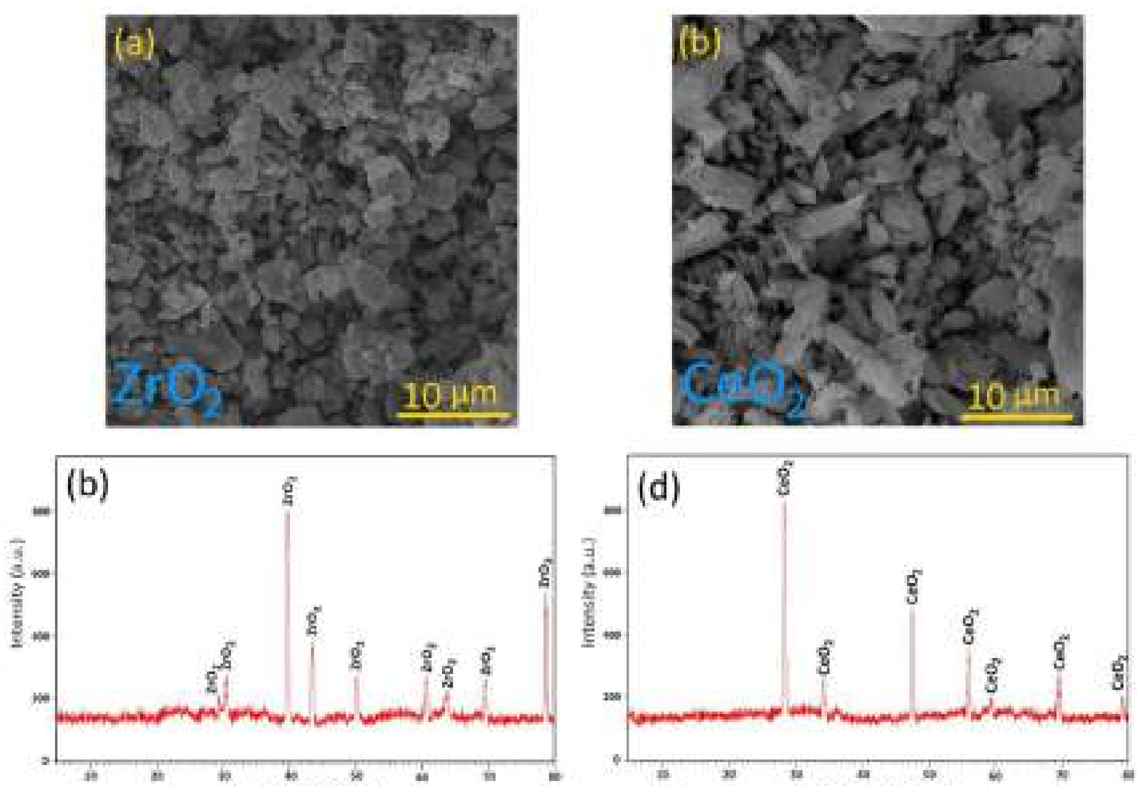

Fig. 1 – SE–SEM images and XRD patterns of (a), (b) ZrO_2 and (c), (d) CeO_2 powders.

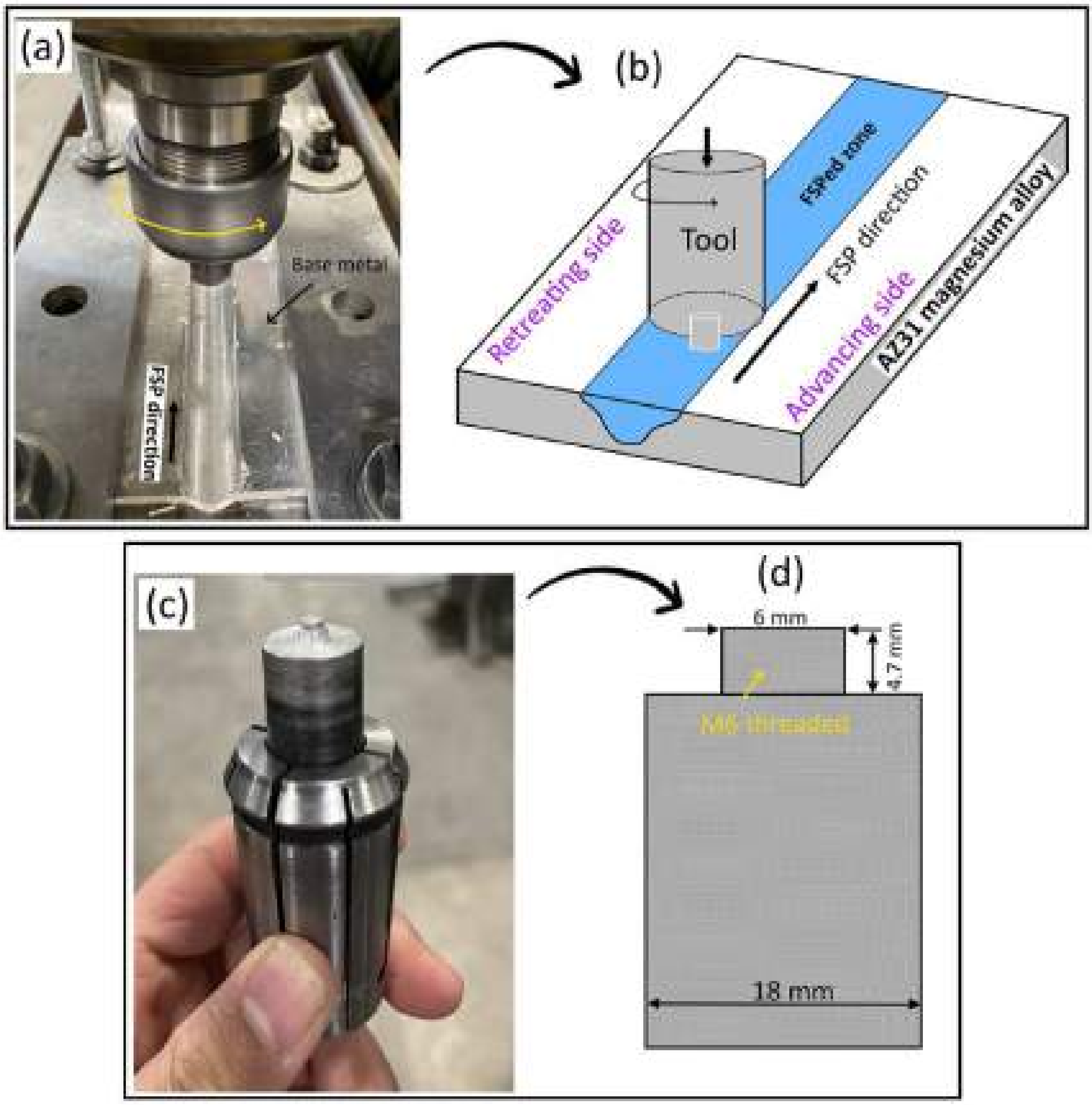

Fig. 2 – FSP processing of AZ31B Mg/ZrO_2+CeO_2 hybrid composite with FSP tool (a), (b) actual and schematic FSP process, and (c) welding tool, (d) dimensions of the welding tool.

The AZ31B Mg/ZrO_2+CeO_2 hybrid composites were developed by employing the FSP method. Before the FSP process, the machining of a narrow rectangular cut section on the AZ31B Mg alloy was carried out. The depth and width of the cut section (groove) were 3 mm and 0.5 mm respectively. This cut section was first filled with the ZrO_2+CeO_2 particulates and then closed up by the H13 probe-less tool-induced shallow plastic deformation effect during the preliminary FSP processing. A cylindrical probe-assisted tool was then utilized for the dispersion of the ZrO_2+CeO_2 particulates in the AZ31B Mg alloy to form the hybrid composite. The actual and schematic representations of the FSP processing of the composites are shown in Fig. 2a and c respectively while the pictorial image, as well as the tool's dimensions, are provided in Fig. 2c and d respectively. The rotating speed of the FSP tool was varied between 800 and 1200 rpm for the surface composite development while the levels of the tool's traverse speed and the tilt angle were constant (100 mm/min and 3°).

The cross-sectional samples of the hybrid composite were obtained after EDM wire cutting. These samples were mounted in resin and underwent metallographic preparations such as grinding with 80–3000 grit papers and polishing with 1-μm diamond paste. After a mirror-like appearance was obtained, the samples were then etched in 100 ml ethanol +25 ml water +25 ml acetic acid +2.5 g picric acid. The microstructures of the hybrid composite were studied via the use of optical, scanning, and transmission electron microscopes. Microstructural image processing (MIP) was adopted for the analysis of the grain and particle sizes in the hybrid composite. The composite samples viewed in TEM were specially prepared via ion beam etching and the samples were then observed in JEOL JEM 2100 TEM. The mechanical tests performed on the hybrid

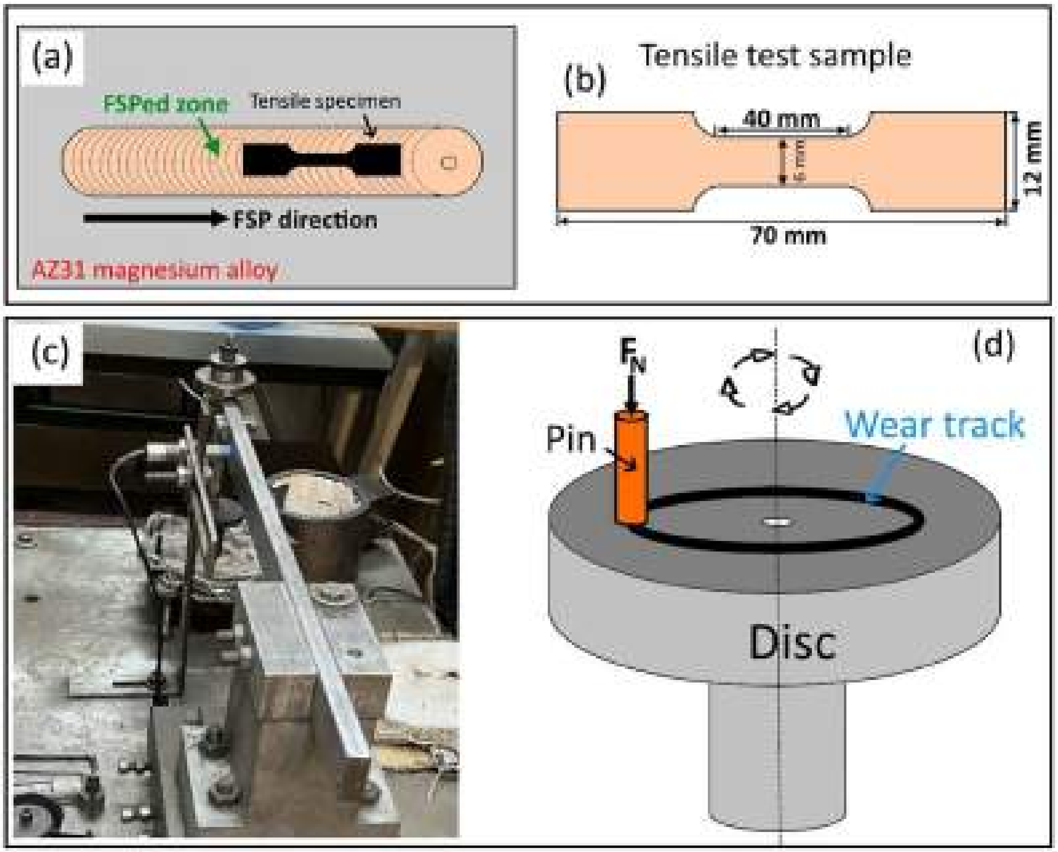

Fig. 3 – (a) Tensile sample location, (b) dimensions of the tensile sample, (c) wear test setup, (d) schematic representation of wear operation.

composite include microhardness, wear, tensile, corrosion, and shear punch tests. The microhardness values across the hybrid composite were determined by employing the Vickers test (50 g load and 10 s time). Fig. 3a shows the location from which the tensile sample was taken while the tensile sample's dimensions are shown in Fig. 3b. Pin-on-disk wear tests were carried out on the developed AZ31B Mg/ZrO_2+CeO_2 hybrid composites as shown in Fig. 3c and d. Table 3 provides the details of the parameters employed for the wear test. Following the ASTM E8M standard, the tensile strengths of the hybrid composite were determined. The test was performed at a constant speed of 1 mm/min on an INSTRON 5500R universal tensile machine (see Fig. 4a). The shear punch tests (SPT) were performed on the AZ31B Mg/ZrO_2+CeO_2 hybrid composites with a strain rate of 10^{-3} at laboratory temperature on a SANTAM SPT machine. The SPT process showing the punch and dies setup is illustrated in Fig. 4b.

From the AZ31B Mg/ZrO_2+CeO_2 hybrid composites, the corrosion samples having dimensions of 5 mm × 5 mm were obtained by EDM. The corrosion samples were ground and subsequently polished before the commencement of the electrochemical test. A 3-electrode electrochemical cell system was utilized for the corrosion test in a 3.5% brine (NaCl) solution. The working, counter, and reference electrodes for the corrosion tests were the composite sample, the platinum, and the saturated calomel electrodes respectively. The corrosion properties i.e., corrosion potentials and current densities of the AZ31B Mg/ZrO_2+CeO_2 hybrid composites were employed for the appraisal of the corrosion behaviour/resistance of the AZ31B Mg/ZrO_2+CeO_2 hybrid composites. After the corrosion test, the samples were further studied in a scanning electron microscope (SEM).

3. Results and discussion

3.1. *Appearance and microstructure*

Fig. 5a–c reveal the surface appearances of the AZ31B Mg/ZrO_2+CeO_2 hybrid composite produced at three dissimilar tool rotational speeds while the matching cross-sections of the composites are revealed in Fig. 5d and e respectively. The

Table 3 – Wear parameters employed for the hybrid composite.

Pin shape	Applied force/N	Sliding velocities/($cm \cdot s^{-1}$)	Pin diameter/cm	Pin rotating speed/($r \cdot min^{-1}$)	Temperature /C
Cylindrical	40	35	1	26.04	25 ± 1

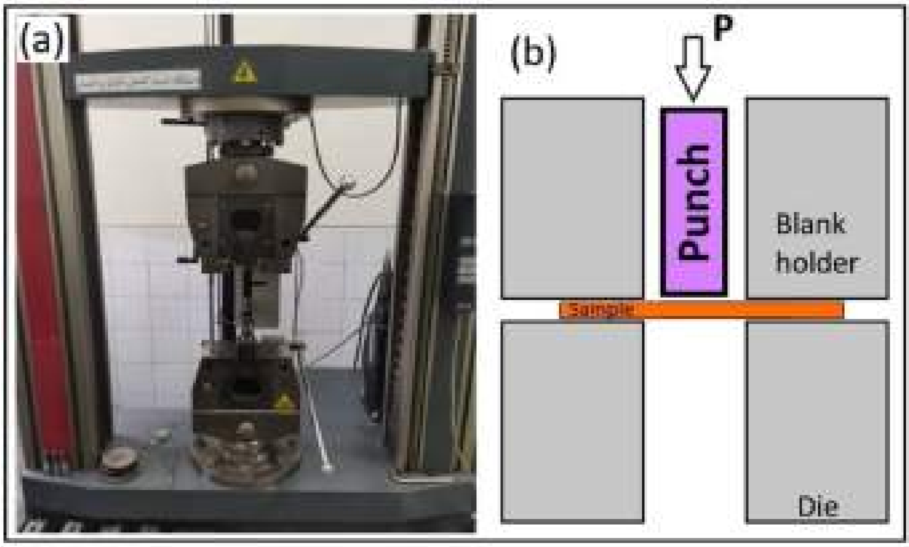

Fig. 4 – Loadbearing tests on the FSP'ed AZ31B Mg/ZrO_2+CeO_2 hybrid composite (a) tensile testing process, (b) shear punch test.

ripples/onion rings on the surface of the processed samples become finer as the rotational FSP tool speed is raised from a low level (800 rpm) to 1200 rpm (see Fig. 5a–c). Also, a smoother and more reflective surface appearance is palpable in the samples when the speed is elevated up to 1200 rpm in Fig. 5c. This feature is attributed to the improvement in the inherent heat input-assisted material flow during the FSP processing of the AZ31B Mg/ZrO_2+CeO_2 hybrid composite. A direct correlation has been established to exist between the rotation speed and heat input during either the friction stir welding or the processing of materials [32,33].

Higher tool rotational speed thus generates higher plastic straining and viscoplastic-induced heat input required to aid sufficient material flow. It is adjudged that sufficient heat

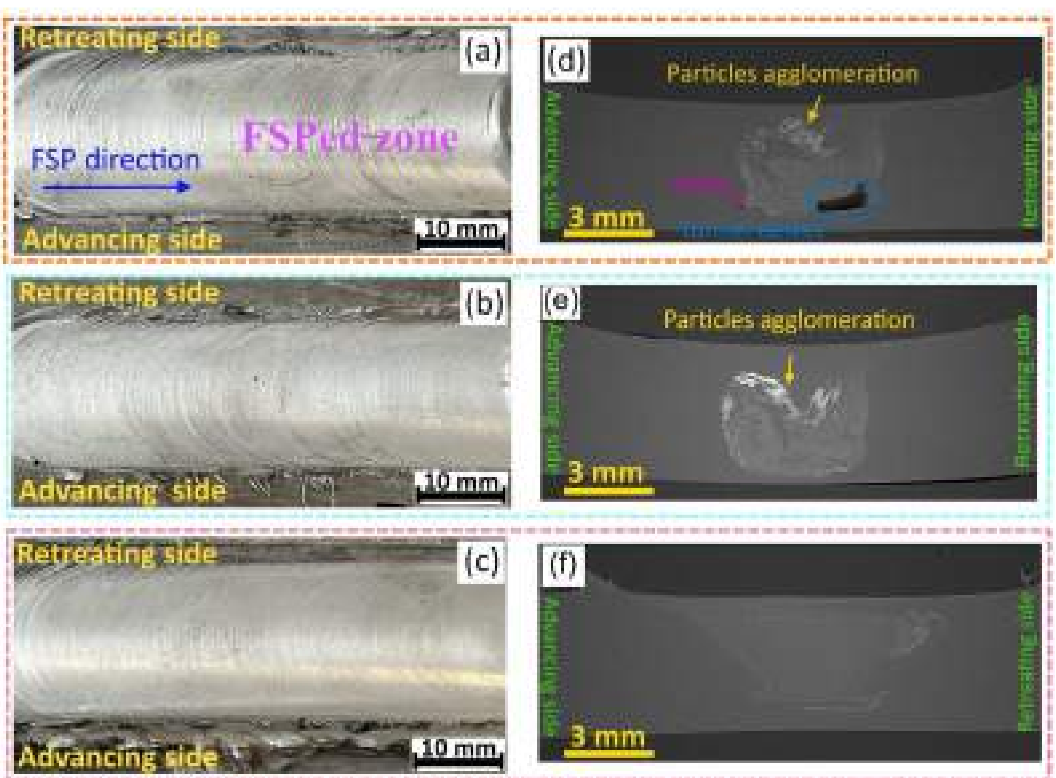

Fig. 5 – Surface appearance and cross-sections of FSP'ed AZ31B Mg/ZrO_2+CeO_2 hybrid composite at (a,d) 800 rpm, (b,e) 1000 rpm, and (c,f) 1200 rpm.

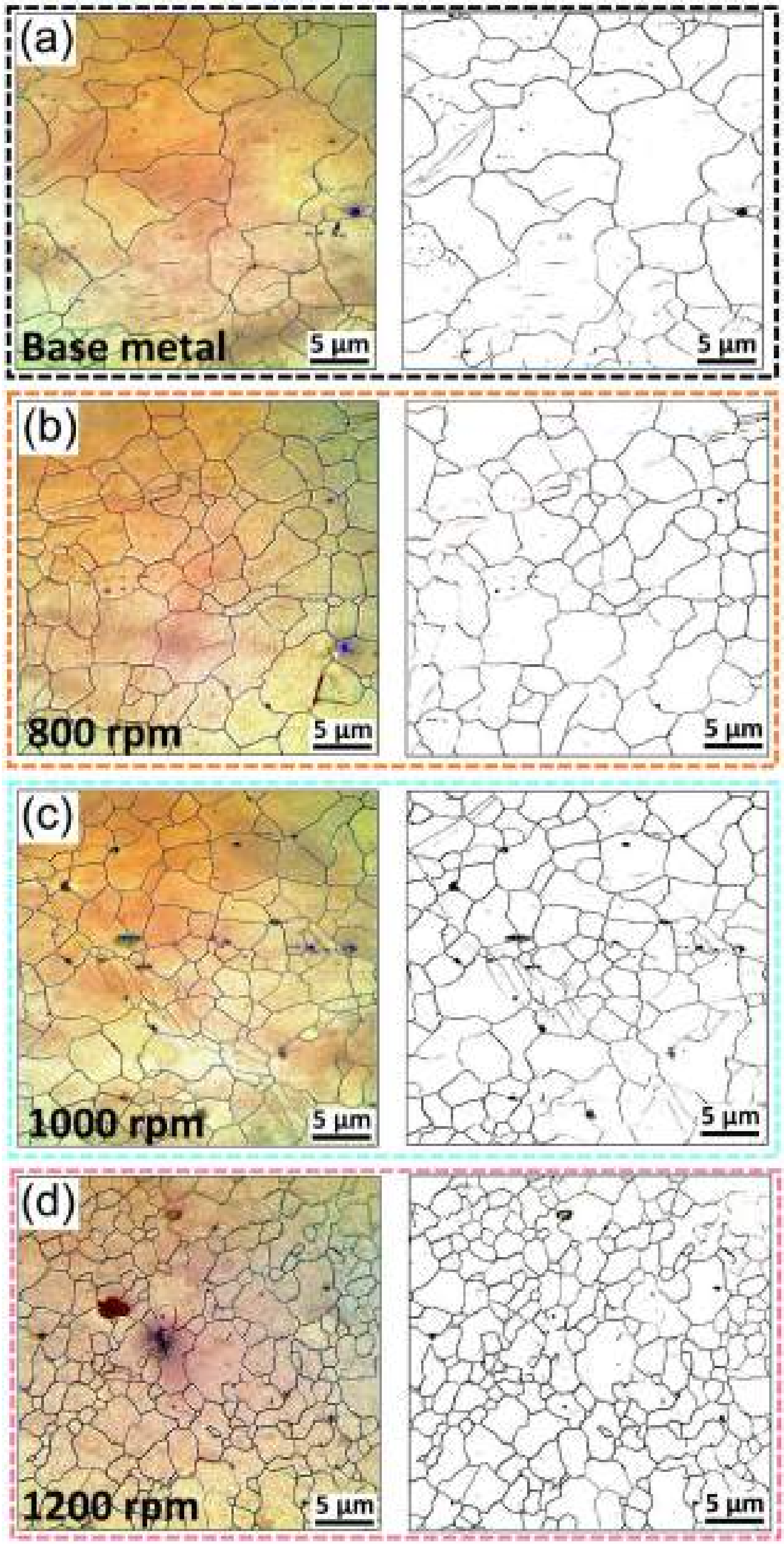

Fig. 6 – Optical Microstructures (OM) of the AZ31B Mg/ZrO_2+CeO_2 hybrid composite (a) base metal, and after processing at (b) 800 rpm, (c) 1000 rpm and (d) 1200 rpm.

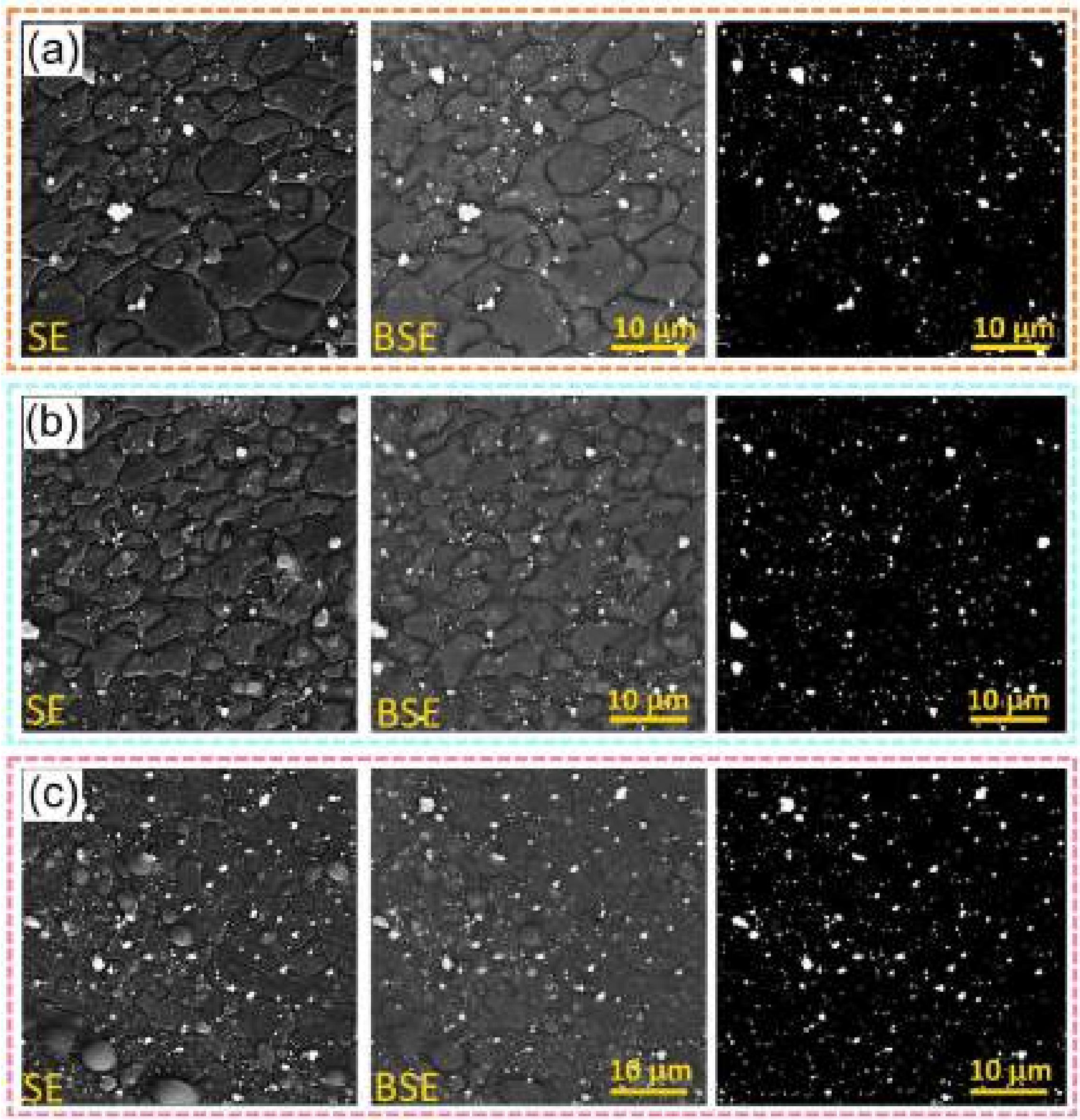

Fig. 7 — FE-SEM images of the AZ31B Mg/ZrO_2+CeO_2 hybrid composite showing particle dispersion (a) 800 rpm, (b) 1000 rpm, and (c) 1200 rpm.

input is generated to aid better material flowability and the resultant smooth surface appearance in Fig. 5c. Meanwhile, the cross-sections of the AZ31B Mg/ZrO_2+CeO_2 hybrid composite showed a disparity in terms of particle agglomeration and inherent flow-related defects as the rotational FSP tool speed was increased (see Fig. 5d and e). Voids, tunnel defect, and ZrO_2+CeO_2 particle agglomeration were found in the 800 rpm-processed samples (see Fig. 5d) because of the likely inadequate heat input and material flow. The flow-related defects (voids, and tunnel) were eliminated in the AZ31B Mg/ZrO_2+CeO_2 hybrid composite as the speed was increased to 1000 rpm in Fig. 5e but the agglomeration of the particles could not be prevented. The deformation ability and the fluidity of the Mg matrix (AZ31B) are enhanced by sufficient heat input or heating process to prevent the formation of voids in the AZ31B-based composites [34]. An additional increase in the rotating speed to 1200 rpm was revealed to have produced properly dispersed ZrO_2+CeO_2 particulates within the AZ31B Mg matrix in Fig. 5f. The elimination of particle agglomeration and flow-related defects in Fig. 5f is linked to sufficient heat input and material plasticity/flow during the FSP processing of the AZ31B Mg/ZrO_2+CeO_2 hybrid composite. The coarse grains of the as-received AZ31B Mg alloy (see Fig. 6a) underwent severe plastic deformation during the development of the AZ31B Mg/ZrO_2+CeO_2 hybrid composite. The resultant microstructures of the FSP'ed samples are equiaxed (see Fig. 6b–d) but there is a noticeable difference in the sizes of the equiaxed grains as the levels of the speed was changed. The formation of the recrystallized and equiaxed grains in the composite is mainly due to the severe plastic deformation and dynamic recrystallization phenomena. Based on the visual assessment, the grain sizes of the developed AZ31B Mg/ZrO_2+CeO_2 hybrid

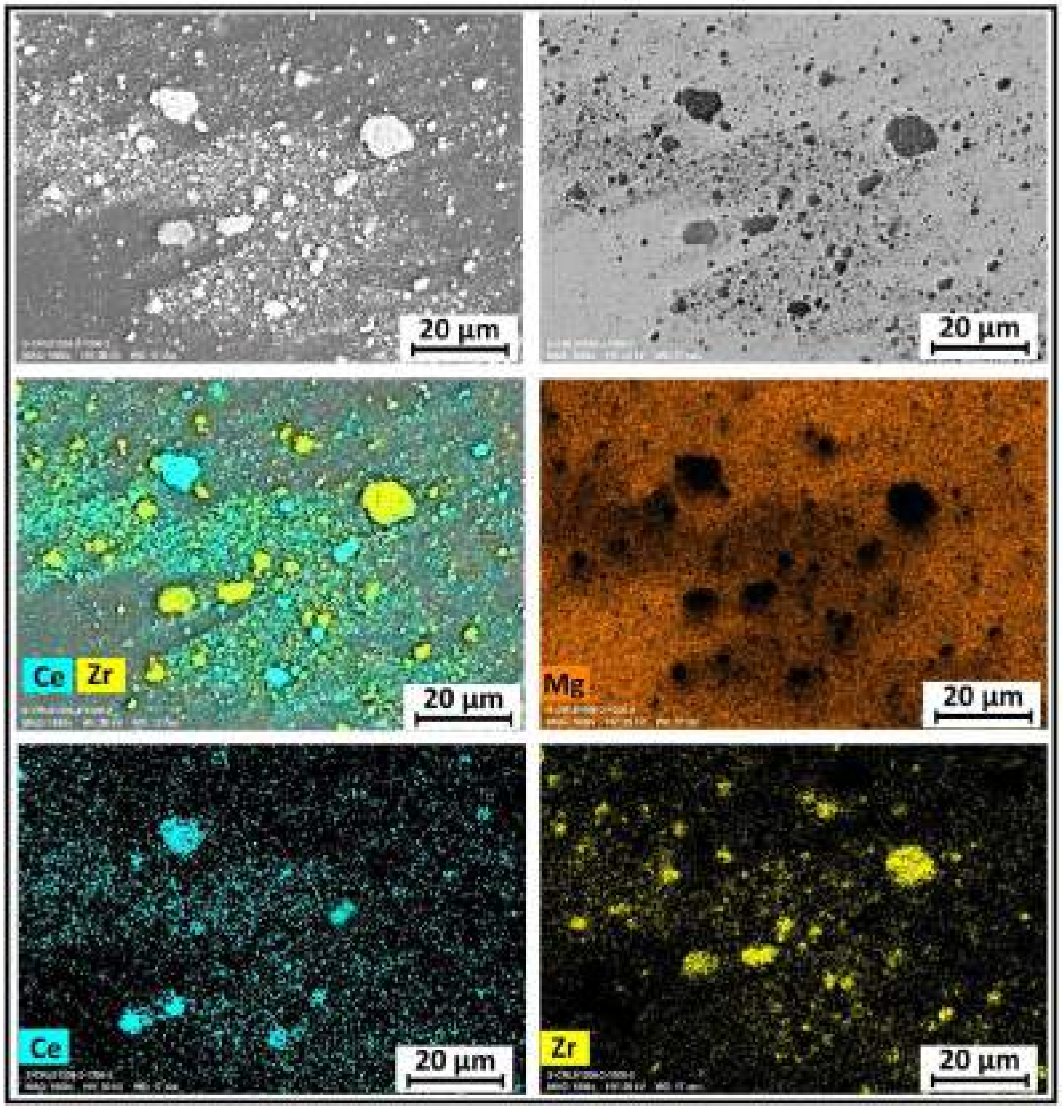

Fig. 8 – EDS mapping of the AZ31B Mg/ZrO_2+CeO_2 hybrid composite processed at 800 rpm.

composite decreased as the tool's rotating speed was increased from low level (see Fig. 6b) to 1200 rpm (see Fig. 6d). This is contrary to the norms in friction stir processing of materials as grain coarsening did not ensue with the elevation of the tool's rotating speed or heat input. This outcome is consequently linked to the presence of the ZrO_2+CeO_2 particles as reinforcements in the AZ31B Mg alloy. The presence of the reinforcements at the grain boundaries of the Mg alloy could have inhibited grain growth, thereby, causing the recrystallized Mg grains to retain their sizes after FSP processing. However, the particle dispersion in the AZ31B Mg could not be efficiently identified in the optical images provided in Fig. 6b–d.

The FE-SEM images of the respective hybrid composite samples were subsequently obtained for the clear discernibility of the embedded ZrO_2+CeO_2 particles in the AZ31B Mg matrix. Evidence of better ZrO_2+CeO_2 particle dispersion (see the whitish spots in Fig. 7) is found in the samples as the processing speed was elevated from the low level (800 rpm) to the high level (1200 rpm).

The uniform dispersal of the reinforced ZrO_2+CeO_2 particles in the AZ31B Mg matrix is enhanced as the speed is elevated from 800 (see Fig. 7a) to 1200 rpm (see Fig. 7c). According to the EDS mapping results, the major elements found in the AZ31B Mg/ZrO_2+CeO_2 hybrid composite are Zr (yellow), Ce (light blue), and Mg (orange) in Figs. 8 and 9. The EDS mapping further confirmed that the whitish spots found in the FE-SEM images as a blend of Ce and Zr elements in Figs. 8 and 9. This validates the dispersion of the ZrO_2+CeO_2 particles within the AZ31B Mg matrix of the composite. The reinforced particle sizes significantly diminished in Fig. 9 (1200 rpm) as compared to Fig. 8 (800 rpm) due to the higher rotating tool-induced plastic straining effect. This effect is reckoned to have favoured particle disintegration and even dispersion during the FSP-processing of the AZ31B Mg/ZrO_2+CeO_2 hybrid composite. The quantitative analysis of the inherent particles in the matrix as well as the resultant grain distribution/sizes in the AZ31B Mg/ZrO_2+CeO_2 hybrid composite was carried out.

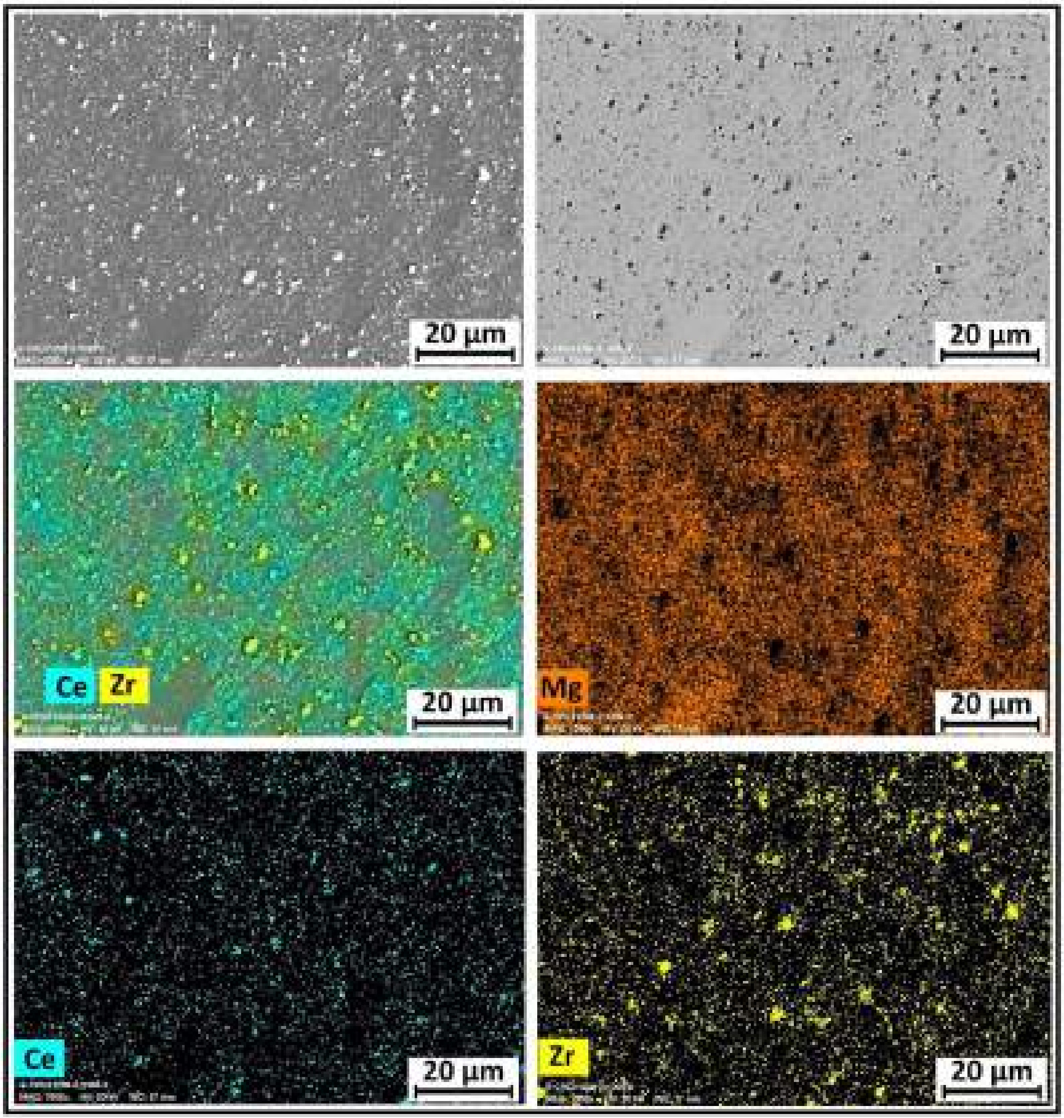

Fig. 9 – EDS mapping of the AZ31B Mg/ZrO_2+CeO_2 hybrid composite processed at 1200 rpm.

The microstructural image processing of the AZ31B Mg/ZrO_2+CeO_2 hybrid composite was carried out to obtain quantitative information about the particle and grain distributions as well as their mean sizes. The distribution and mean sizes of the ZrO_2+CeO_2 particle and grains of the composite are presented in Fig. 10. The mean ZrO_2+CeO_2 particle sizes reduced from 4.52 µm to 2.49 µm as the speed was elevated from low level (800 rpm) to 1200 rpm while the corresponding average grain sizes of the AZ31B Mg/ZrO_2+CeO_2 hybrid composite also reduced from 7.39 µm to 3.38 µm respectively. Intensified dynamic recrystallization was reported as a factor responsible for the appreciable decrease in grain size as the speed was increased from 700 to 1000 rpm in the studies of Harwani et al. [35]. The enhancement in the plastic straining effect, as the tool rotational speed is raised, is a notable phenomenon responsible for the disintegration of the ZrO_2+CeO_2 particles with the increment in the level of the speed in rpm. Dinaharan et al. [36] reported that particle breakages are attributable to severe plastic strain effects during the FSP process. The fine ZrO_2+CeO_2 particles could have acted as restraining particles in the recrystallized AZ31B Mg matrix to impede grain boundary movement and eventual grain growth. Meanwhile, Zenner pinning effect and dynamic recrystallization are reckoned as mechanisms responsible for the refinement of the grains in the AZ31B Mg/ZrO_2+CeO_2 hybrid composite when the speed was elevated from low level (800 rpm) to 1200 rpm.

The peaks of the ZrO_2, CeO_2, and Mg are found in the XRD results of the AZ31B Mg/ZrO_2+CeO_2 hybrid composite in Fig. 11. This is an indication that the chemical reaction between the matrix and the reinforcement did not take place during the FSP-processing of the AZ31B Mg/ZrO_2+CeO_2 hybrid composite. However, the resultant peaks of the phases slightly declined with the upsurge in the level of the tool's rotational speed in Fig. 11. Higher rotating speed (in rpm) was reported to have caused the precipitation and even dispersion of the β-$Al_{12}Mg_{17}$ phase in the FSP'ed AZ31 Mg alloy (without reinforcement) due to the sufficient heat input [37]. However,

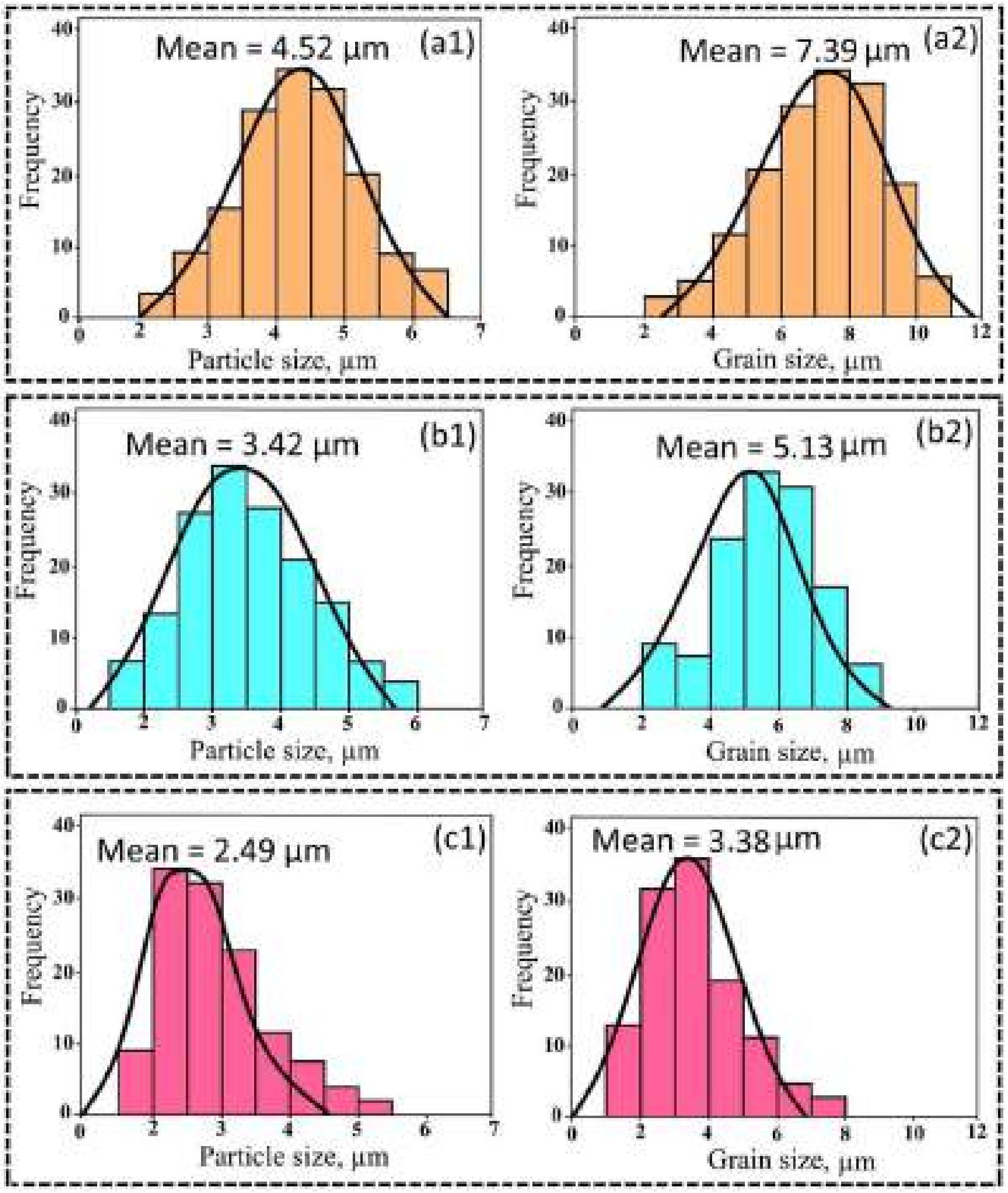

Fig. 10 – MIP processing of the AZ31B Mg/ZrO_2+CeO_2 hybrid composite for quantitative microstructural parameters (a1) particle sizes at 800 rpm, (a2) grain sizes at 800 rpm, (b1) particle sizes at 1000 rpm, (b2) grain sizes at 1000 rpm, (c1) particle sizes at 1200 rpm, (c2) grain sizes at 1200 rpm.

no precipitated phase was detected in the AZ31B Mg/ZrO_2+CeO_2 hybrid composite irrespective of the processing tool speed. This outcome could have been influenced by the inherent ZrO_2+CeO_2 particles in the matrix of the AZ31B Mg alloy. These particles are reckoned to have played a significant role in the straining/strain rate and deformation of the matrix to cut back any chemical reaction or formation of new phases in the composite during the FSP process.

Ce and Zr are heavy atoms relative to Mg. Their atomic numbers are 58 (Ce), and 40 (Zr) while that of Mg is 12. As a result, it is expected that the regions with heavier atoms (more crystalline) are the dark spots/regions in the Bright-Field TEM images while these regions are brighter in the Dark-Field TEM images in Fig. 12. The dark and bright/whitish spots (see Fig. 12) are the embedded ZrO_2+CeO_2 particles in the matrix of the AZ31B magnesium alloy in the Bright and Dark-field TEM images respectively. Even distribution and reduced sizes of the ZrO_2+CeO_2 particles are found in Fig. 12b (1200 rpm) as compared to Fig. 12a (800 rpm). This result further validates the results presented in Figs. 7–10. In the Bright-Field TEM images, dislocation appearances are palpable around the large/clustered particles in Fig. 12a and the recrystallized Mg matrix in Fig. 12b. The differential straining between the ZrO_2+CeO_2 particles and the Mg matrix could be responsible for the observed dislocation in Fig. 12a while sub-grains aided dislocations could be a factor for that in Fig. 12b. The images

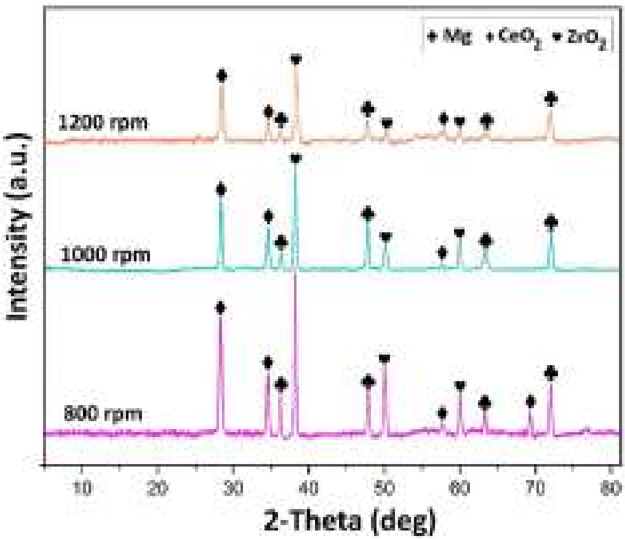

Fig. 11 – XRD results of the AZ31B Mg/ZrO_2+CeO_2 hybrid composite.

did not reveal any proof of particle-matrix diffusion because of the discrete nature of the interfaces of the ZrO_2+CeO_2 particles and the AZ31B Mg matrix [38].

3.2. *Mechanical properties*

3.2.1. *Hardness*

Fig. 13 shows the plots of the microhardness values across the AZ31B Mg/ZrO_2+CeO_2 hybrid composite after different rotational speeds of the FSP tool. The microhardness values increase towards the stirred center of the composite. The maximum hardness is obtained at the stirred center of the composite. The maximum hardness values of 99, 122, and 135 HV were attained in the composite samples fabricated with 800, 1000, and 1200 rpm speeds respectively. This finding is owing to the direct correlation between grain/particle refinement and the tool's rotating speed. The composite sample with the finest grain and particle refinement produced the highest microhardness response. This is linked to the Hall Petch effect and inhibition of dislocation movement during the indentation process. The factors responsible for hardness improvement in composites have been enlisted as high dislocation density, the better density of reinforced particles, reduced grain size, and particle content [39]. In this study, the refinement of the ZrO_2+CeO_2 particles is reckoned to be a major factor for the hardness improvement after the increment in the rotational speed's level. The fine and uniformly dispersed ZrO_2+CeO_2 particles are believed to have aided the restriction of indentation force/pressure and deformation (dislocation movement) during the hardness test. In some studies, the inherent geometrically necessary dislocations are induced by the FSP process to enforce an improvement in hardness properties [39]. As a result, the mechanism for the improvement in hardness in this study is linked to the grain-size strengthening phenomenon.

Thermal softening attributable to a higher rotating speed level (heat input) was absent in Fig. 13 due to the inherent ZrO_2+CeO_2 particles in the AZ31B Mg matrix. The combination of fine hard particles and high density of dislocation was reported to have impeded the thermal softening effect related to the FSP process in the studies of Paidar et al. [38]. It has been reported that the softness (reduced hardness value) of magnesium alloy's base metal is owing to its {0001} β-fiber texture while the {0001} basal slip and non-basal slip such as {1010} prismatic and {112} pyramidal slips may occur as mechanisms of deformation in Mg alloys during the FSP process [40]. The SZ's microhardness of the composite improved significantly due to the synergy of dynamic recrystallization and reinforced ZrO_2+CeO_2 particles. The particle-stimulated nucleation could have aided the hardness improvement in the AZ31B Mg/ZrO_2+CeO_2 hybrid composite [10,41]. Mazaheri et al. [21] attributed the improvement in the hardness of the AZ31/ZrO_2 composite to the grain-boundary strengthening mechanism promoted by the refined grains. Particles' non-uniform distribution and agglomeration were also reported to have caused variation in microhardness in the works of Patel et al. [42].

3.2.2. *Shear properties*

The shear strength-displacement curves of the AZ31B Mg/ZrO_2+CeO_2 hybrid composite fabricated at dissimilar rotating speeds are revealed in Fig. 14. The punching shear strengths of the AZ31B Mg/ZrO_2+CeO_2 hybrid composites fabricated at 800 rpm, 1000 rpm, and 1200 rpm were 121, 178, and 237 MPa respectively. The area under the shear strength-displacement curve is also enhanced as the rotating speed was increased for the development of the AZ31B Mg/ZrO_2+CeO_2 hybrid composite. The observed results can be attributed to the effects of material flow, particle dispersion and size, and defects. Insufficient material flow, particle agglomeration, and the presence of voids and tunnels are unfavorable features of the 800 rpm-processed composite. These features are inherent stress concentration zones that could have aided the quick shearing of the sample during shear punch testing. However, sufficient material flow aided better dispersion of the ZrO_2+CeO_2 particles and eliminated defects such as voids and tunnels in the 1200 rpm-processed composite. This observation is associated with the improvement in the shear strength of the AZ31B Mg/ZrO_2+CeO_2 hybrid composite. In the studies of Liu et al. [43], it was reported that the shearing strength of the reinforced Al–Al joint was meaningfully enhanced via the dislocation-strengthening mechanism introduced by the embedded fine B_4C particles. There is a direct relationship between the mean ZrO_2+CeO_2 particle sizes and the punching shear strength of the AZ31B Mg/ZrO_2+CeO_2 hybrid composite. It was acknowledged that the fine ZrO_2+CeO_2 particle-assisted dislocation strengthening was accountable for the significant shear resistance of the AA6061/316 steel-reinforced composites in the works of Liu et al. [44]. As a result, it can be concluded that finer ZrO_2+CeO_2 particles hinder dislocation movement in the AZ31B Mg/ZrO_2+CeO_2 hybrid composite during the shear punching test. According to Bai et al. [3], the basal texture of the GNP-reinforced AZ31 Mg was stronger after the FSP process, leading to grain refinement and particle-assisted strengthening effects. These effects eventually caused an improvement in the mechanical properties of the composite as the particles aided better load transfer. Better dispersion of ZrO_2+CeO_2 particles and

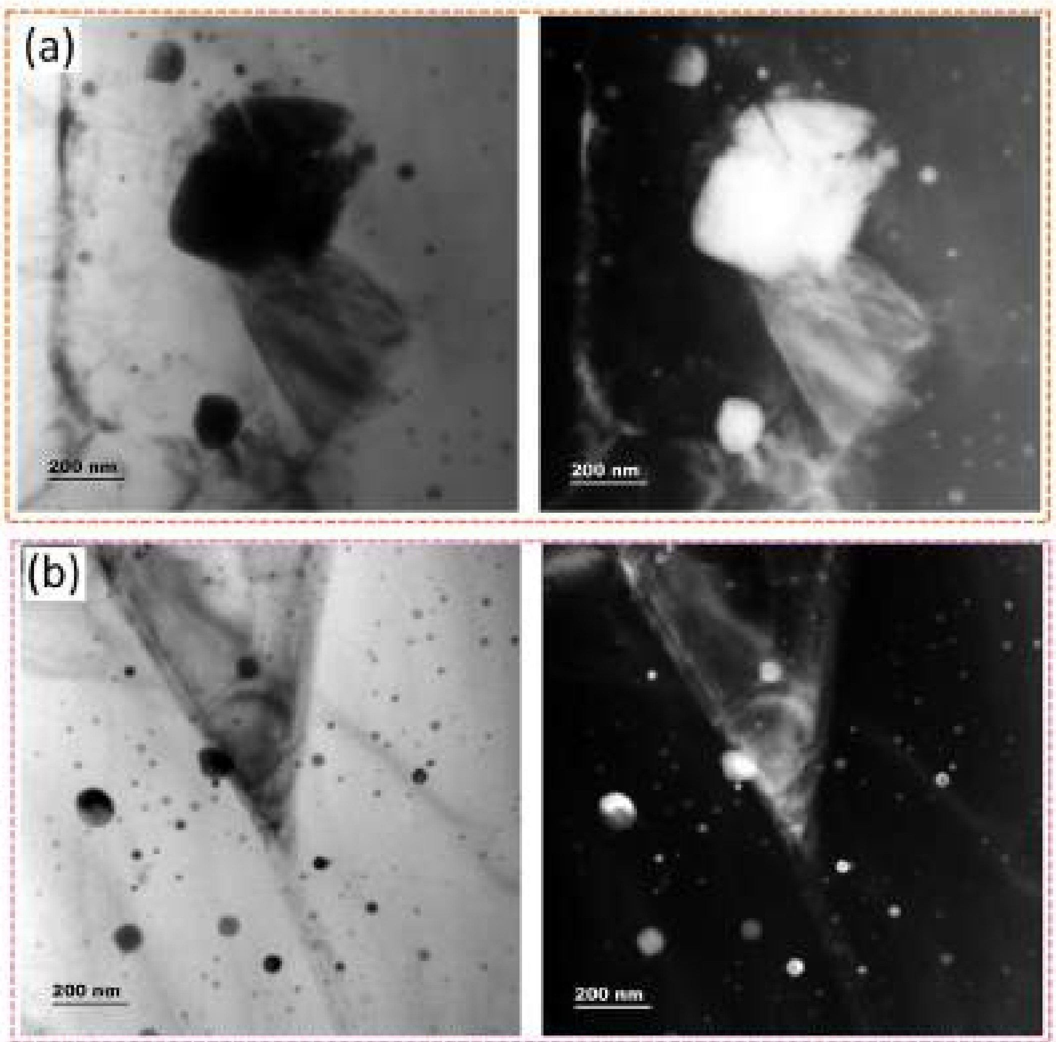

Fig. 12 – Bright and dark field TEM images of the AZ31B Mg/ZrO_2+CeO_2 hybrid composite processed at (a) 800 rpm, and (b) 1200 rpm.

textural transformation of the composite due to the FSP process could also have influenced the shearing or loadbearing performance of the AZ31B Mg/ZrO_2+CeO_2 hybrid composite.

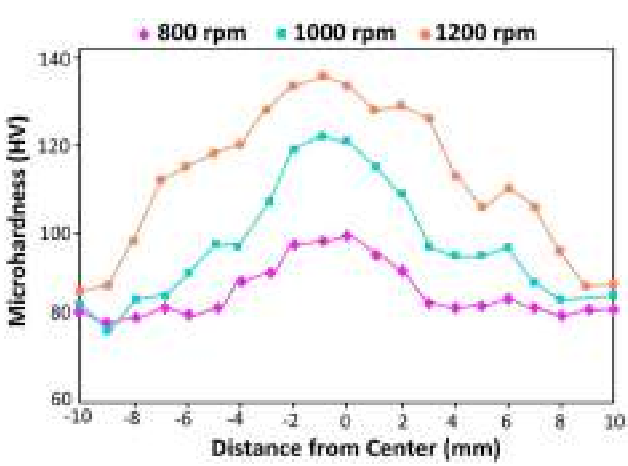

Fig. 13 – Microhardness distribution across the AZ31B Mg/ZrO_2+CeO_2 hybrid composite at different rotating speeds.

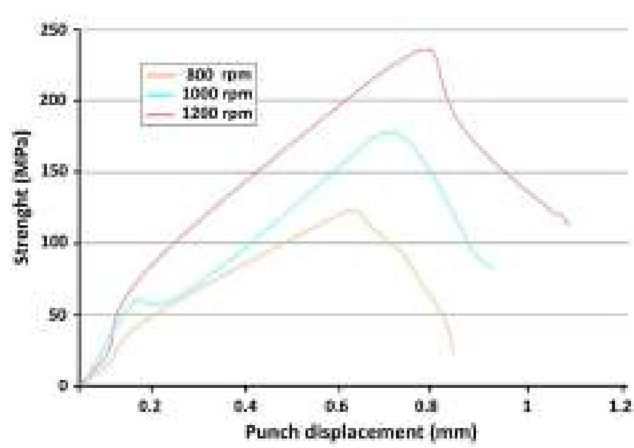

Fig. 14 – Shear strength against punch displacement of the AZ31B Mg/ZrO_2+CeO_2 hybrid composite.

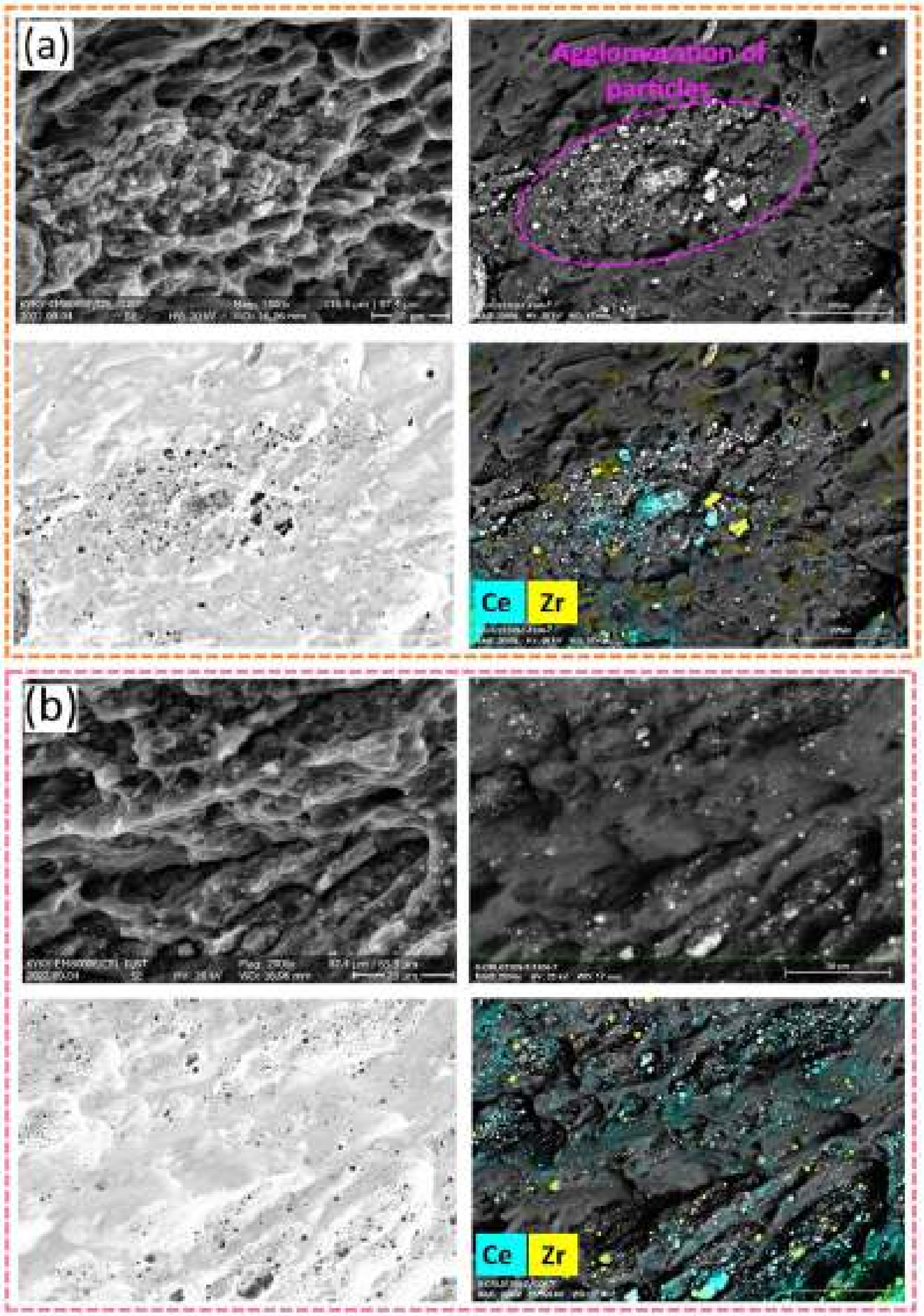

Fig. 15 – Fracture surfaces of the AZ31B Mg/ZrO_2+CeO_2 hybrid composite after SPT (a) 800 rpm and (b) 1200 rpm.

The fractured surfaces of the hybrid composite after the SPT tests with their respective EDS mapping are provided in Fig. 15. The sheared (fractured) surfaces in Fig. 15a (800 rpm) and Fig. 15b (1200 rpm) are uneven, which is an indication of multiple shearing paths in the composite. The presence of multi-shear planes in the shear samples has been linked to the fracture resistance encountered during the shear punching of the composite [45]. Dimple-like appearances and shear lips are prominent in Fig. 15a and b, which is an indication of some resistance to shearing during the SPT tests. Based on the EDS map in Fig. 15a, the regions with a substantial level of dimples are areas with little or no ZrO_2+CeO_2 particles. This

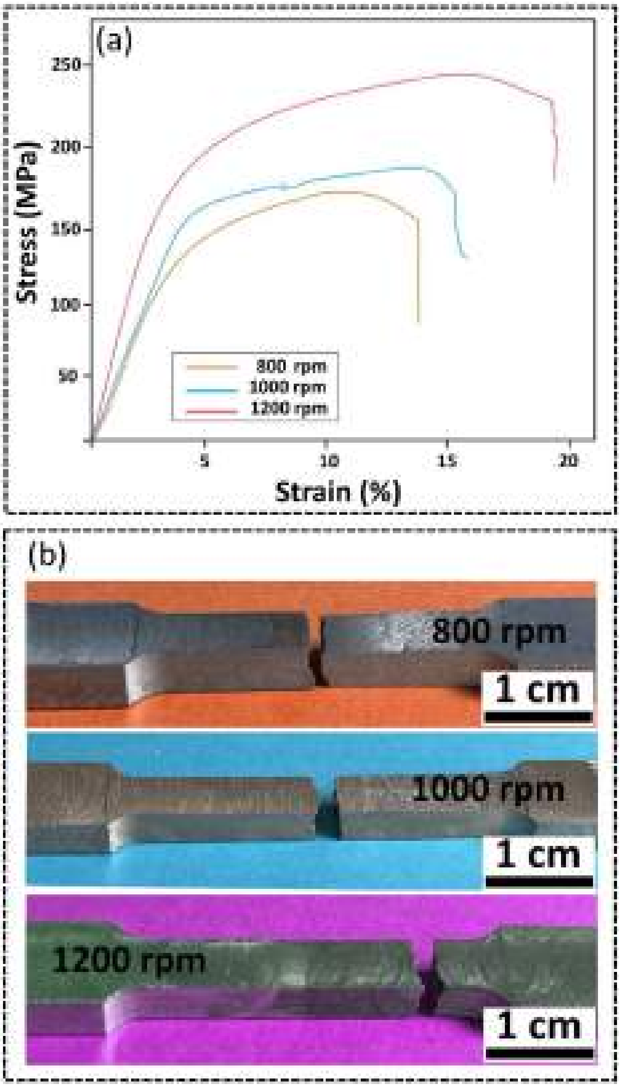

Fig. 16 – Tensile test results of the AZ31B Mg/ZrO_2+CeO_2 hybrid composite (a) stress-strain curves, (b) fractured samples.

shows that particle-assisted dislocation strengthening may not have occurred at the region during the SPT test. However, the distribution level and sizes of the ZrO_2+CeO_2 particles in the composite are observed to have influenced the fracture mode of the composite. The sheared region with agglomerated particles reveals the presence of a brittle appearance in Fig. 15a (800 rpm) while such observation is not found in the 1200 rpm-processed composite (see Fig. 15b). These findings are in agreement with the shear strength-displacement curves in Fig. 14.

3.3. *Tensile properties*

The tensile results of the AZ31B Mg/ZrO_2+CeO_2 hybrid composite developed at different tool speeds are shown in Fig. 16. Fig. 16a shows the stress-strain curves while the fractured locations of the composite are revealed in Fig. 16b. Improvement in the tensile strength/stress is recorded when the level of the rotating speed is increased from low level (800 rpm) to 1200 rpm. The tensile stress/strengths of 228 MPa (1200 rpm), 186 MPa (1000 rpm), and 172 MPa (800 rpm). This observation follows the same trend as the SPT results. The 1200 rpm-processed composite sample had no stress raisers such as particle agglomeration, voids, and tunnel defect (see Fig. 5) as compared to the other composite samples owing to the improved material flow and ZrO_2+CeO_2 particle distribution. The absence of these stress concentration sites in the 1200 rpm-processed composite is a dominant factor for the significant improvement in the tensile strength of the AZ31B Mg/ZrO_2+CeO_2 hybrid composite while the presence of somewhat particle agglomeration slightly reduces the tensile strength of the 1000 rpm-processed sample. The weakest tensile strength is recorded in the 800 rpm-processed sample due to the presence of the abovementioned defects (particle agglomeration, voids, and tunnel defect). This outcome agrees with the works of Sharma et al. [11] and Dinaharan et al. [46]. The agglomerated graphene particulates at the grain boundaries of the AZ31/MWCNTS/Graphene hybrid nanocomposite were reported to have reduced tensile strength of the composite [11] while the clusters Ti particulate reduced the tensile behaviours of the AZ31/Ti composite [46]. From another perspective, the finer and uniformly dispersed ZrO_2+CeO_2 particles are considered to have supported dislocation pinning in the composite during the tensile test. As it is expected, the recrystallized or finer grains imply that there is a direct increase in the volume of the grain boundaries in the 1200 rpm-processed composites. The presence of finer ZrO_2+CeO_2 particles at the grain boundaries of the composite is believed to have offered hindrances to dislocation per unit length in the AZ31B Mg/ZrO_2+CeO_2 hybrid composite (1200 rpm) during the tensile test [39]. The presence of refined particles in composites has been acknowledged to cause a delay in stress concentration or aid stress dispersion [38]. This phenomenon is reckoned to have hindered the tendency of forming micro-cracks and premature failure in the composite while improving the load-bearing attribute of the composite. As a result, fine particles-aided dislocation strengthening is considered one of the mechanisms responsible for improved tensile strength. Sufficient inter-material flow, particle dispersion, and dislocation tangles were reported as the important factors for the improvement of the tensile strengths of particle-reinforced alloy [47]. The inherent fine WC particles in the reinforced Al/WC nanocomposite have been reported to aid the dislocation strengthening of the composite [48]. Other mechanisms that could be responsible for strengthening in the composites are Orowon strengthening, thermal expansion mismatch-induced dislocation, and recrystallized grains. Similarly, the fracture location of the AZ31B Mg/ZrO_2+CeO_2 hybrid composite after the tensile testing process is revealed in Fig. 16b. The fracture location shifted away from the stirred centre in the 1200 rpm-processed sample after the tensile loading condition. This is obviously due to the resistance of the stirred centre to crack initiation during the tensile test. The fracture location of the 800 rpm-processed samples did not move away from SZ (stir centre) owing to the presence of stress raisers like particle agglomeration, tunnel defect, and voids at the stirred centre of the sample. Likewise, the agglomerated ZrO_2+CeO_2 particles

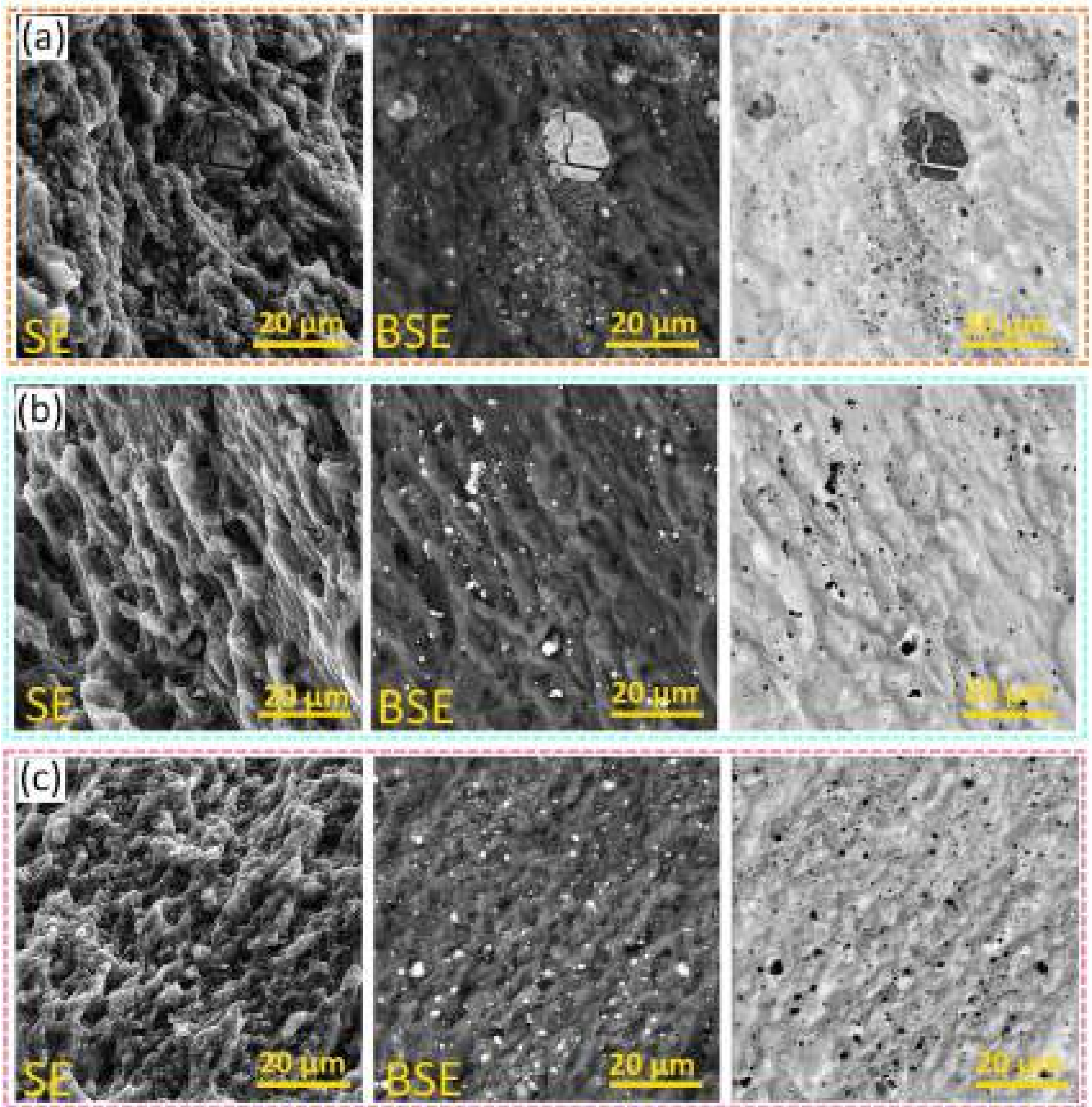

Fig. 17 – Fractures of the AZ31B Mg/ZrO_2+CeO_2 hybrid composite after the tensile test (a) 800 rpm, (b) 1000 rpm, and (c) 1200 rpm.

could be responsible for the failure at the stirred centre of the 1000 rpm-processed composite. To further understand the fracture mode of the samples, the SEM images of the fractured samples were examined.

The fractured surfaces of the tensile samples are provided in Fig. 17 while their XRD results are shown in Fig. 18. Different sizes of the ZrO_2+CeO_2 particles are found on the fractured surfaces of the hybrid composite just like the observed microstructures in Figs. 7–9. The XRD results of the fractured surfaces confirmed the presence of Mg, ZrO_2, and CeO_2 phases (see Fig. 18). This indicates that the reinforced ZrO_2+CeO_2 particles play a noteworthy role in the fracture behaviour of the composites. The assessment of Fig. 17a shows that decohered and brittle-like fracture appearance is dominant.

The large particles in the 800 rpm-processed sample (see Fig. 17a) with inherent voids and tunnel defects are considered easy crack initiation sites that favor the poor load-

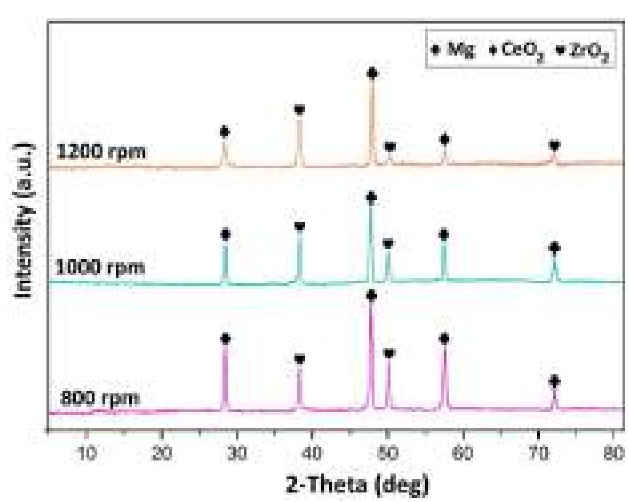

Fig. 18 – XRD results of failed samples.

bearing performance of the composite. However, mixed fracture appearances with little shallow dimples are found in both Fig. 17b and c. These appearances (Fig. 17b and c) are somewhat close due to the absence of dominant stress raisers (voids and tunnels) in the composites. The effect of the disparity in the level of particle distribution on fracture could not be ascertained in Figs. 17b and c even though particle agglomeration was found in the 1000 rpm-processed composite when compared to the 1200 rpm-processed counterpart. However, the improvement in the material flow and the ZrO_2+CeO_2 particle distribution in the 1200 rpm-processed sample is considered the reason for the better tensile strength and area under the tensile stress-strain curve of the composite.

3.4. Tribological behaviour

Figs. 19–22 provide and compare the tribological behaviors (such as weight/wear loss, wear rate, worn surfaces, debris, and friction coefficient) of the hybrid composite. As expected, a direct relationship is found to ensue between the weight loss (wear loss) and the sliding distance (see Fig. 19a). Nevertheless, the least weight (wear) loss is found in the 1200 rpm-processed sample, followed by 1000 rpm and 800 rpm-processed counterparts respectively. The wear rates (in mg/m) are 0.57, 0.39, and 0.28 mg/m for the 800 rpm, 1000 rpm, and 1200 rpm-processed composites respectively in Fig. 19b while their respective specific wear rates are 4.09×10^{-5}, 3.56×10^{-5}, and 2.87×10^{-5} mm^3/Nm respectively (see Table 4). The wear rate (see Fig. 19 and Table 4) is indirectly related to the microhardness values (see Fig. 13) of the hybrid composite, which is an indication of a good agreement with Archard's equation. The improvement in these wear properties (weight loss, wear rate, and specific wear rate) as the rotating speed is increased is linked to the finer ZrO_2+CeO_2 particles and hardness improvement. The self-lubricating properties of the CeO_2 particle could also have influenced the wear properties of the composite. The fine and homogeneously dispersed ZrO_2+CeO_2 particles are considered to have offered better resistance to deformation leading to lesser weight loss and enhanced wear rate/specific wear rate. It is considered that the finely dispersed hard ZrO_2+CeO_2 particles in the AZ31B Mg matrix will bear the direct load on the composite during the wear test to mitigate the weight loss (wear loss) and improve the wear rate of the 1200 rpm-processed composite. A large surface or area fraction with embedded uniformly dispersed ZrO_2+CeO_2 particles will counteract deformation and material (wear) loss in the 1200 rpm-processed composite during the wear test.

The worn surfaces of the AZ31B Mg/ZrO_2+CeO_2 hybrid composite fabricated with dissimilar speeds (800 rpm–1200 rpm) are shown in Fig. 20. The corresponding delaminated regions along the sliding directions on the worn surfaces are indicated in Fig. 20a–c. A large area of the worn surfaces underwent significant wear or delamination in Fig. 20a. This outcome is due to the insufficiently dispersed ZrO_2+CeO_2 particles or particle agglomeration in the Mg matrix. The improperly reinforced or unreinforced regions of the composite are exposed to little or no resistance to deformation and wear (adhesive wear) while the region with the dominant presence of the reinforced ZrO_2+CeO_2 particles experiences abrasive wear in Fig. 20a. The level of delamination declined as the tool's speed was increased to 1000 rpm and 1200 rpm respectively. This is because of the improved plasticized material flow and elimination of particle agglomeration in the composite. More resistance to wear is experienced by the 1200 rpm-processed composite as a result of the fine and homogeneous dispersion of ZrO_2+CeO_2 particulates in the AZ31B matrix. The observed results are in agreement with the tribological properties presented in Fig. 19. The worn debris of the composite is examined to further clarify the influence of the variation in the rotating speed (rpm) on the wear performance (see Fig. 21). The worn debris of the AZ31B Mg/ZrO_2+CeO_2 hybrid composites is revealed in Fig. 21. Irregular-shaped and large wear particles are found in Fig. 21a while a combination of large and fine wear particles is found in Fig. 21b. Predominantly fine wear particles are present in Fig. 21c. As a result, it can be said that the average particle

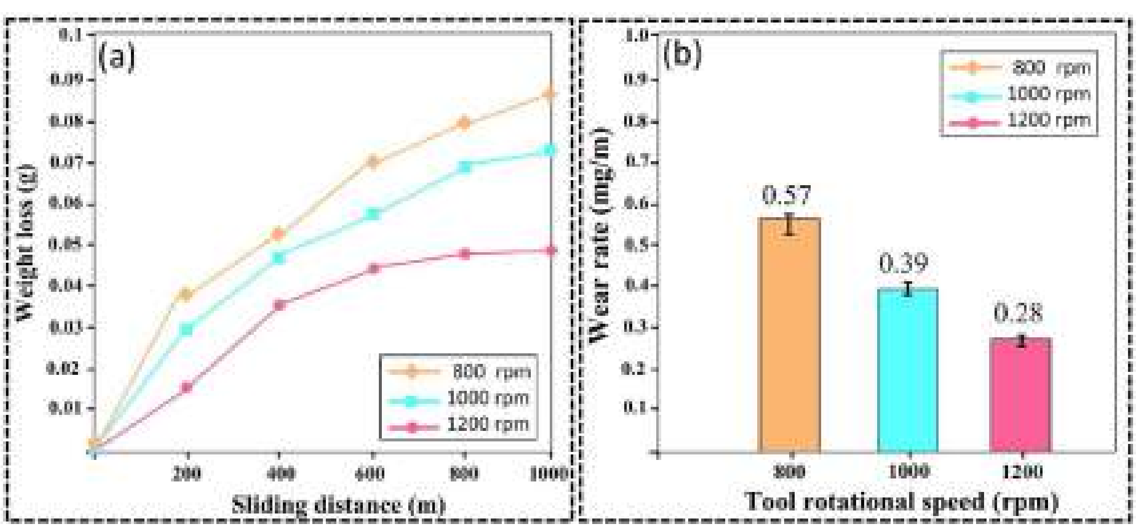

Fig. 19 – Wear results of the AZ31B Mg/ZrO_2+CeO_2 hybrid composite, (a) weight loss vs sliding distance, (b) wear rates.

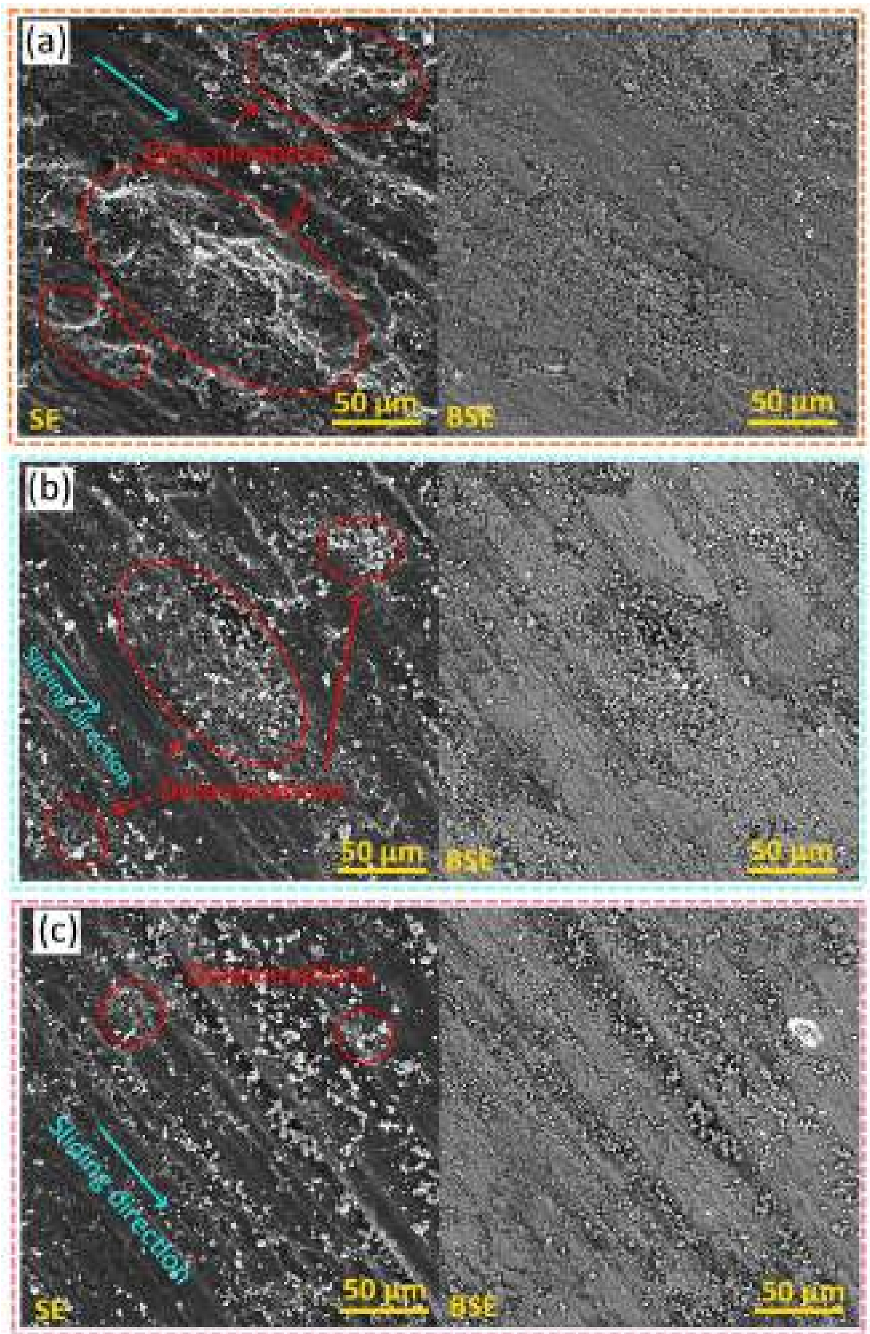

Fig. 20 – Worn surfaces of the AZ31B Mg/ZrO_2+CeO_2 hybrid composite: (a) 800, (b) 1000, and (c) 1200 rpm.

sizes of the wear debris diminished as the rotating speeds of the tool were elevated to 1200 rpm. This is a confirmation that particle agglomeration or poorly dispersed ZrO_2+CeO_2 particles lead to notable wear (weight) loss in the 800 rpm- and 1000 rpm-processed composites while homogeneously dispersed and fine ZrO_2+CeO_2 particles cutback the wear loss or the amount of wear debris produced after the wear test in the AZ31B Mg/ZrO_2+CeO_2 hybrid composite. It is considered that the fine and properly dispersed ZrO_2+CeO_2 particles in the AZ31B matrix prevent the direct contact of the pin and the matrix during the wear test. This occurrence implies that lesser deformation or applied load will be borne by the composite leading to lesser wear debris and improved tribological performance. The increase in the volume of the wear debris has been attributed to tribo-layer instability, severe plastic deformation of the substrate, and loss of particle-strengthening effect in the studies of Moharrami et al. [39].

The friction coefficients of the AZ31B Mg/ZrO_2+CeO_2 hybrid composites are presented in the plots provided in Fig. 22. The fluctuation of the friction coefficient (waveforms) is intense in Fig. 22a and slightly decreased in Fig. 22b while the least fluctuation level is recorded in Fig. 22c. The

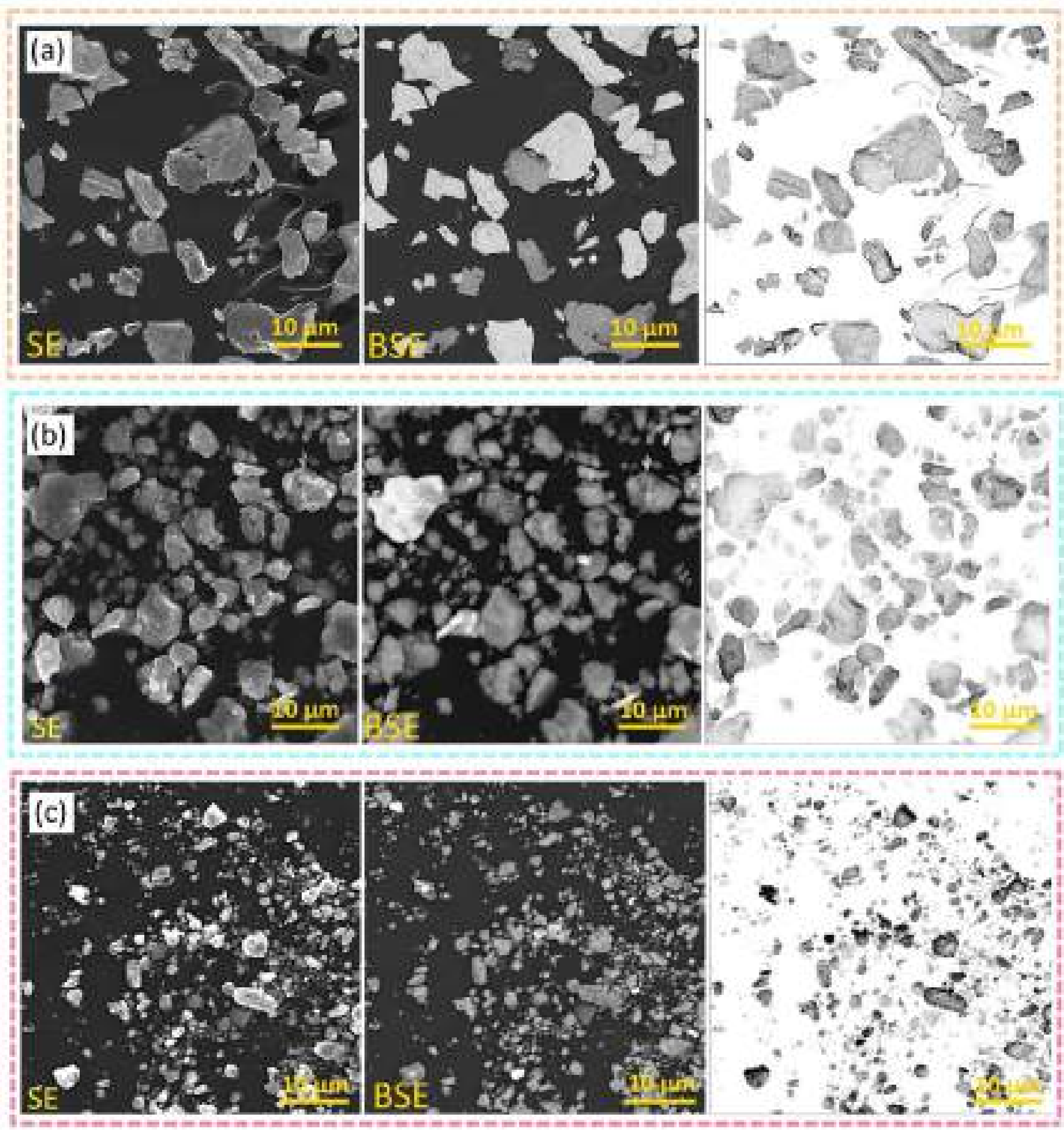

Fig. 21 – Debris produced after wear test for samples processed at (a) 800, (b) 1000, and (c) 1200 rpm.

fluctuations in the friction coefficient may be due to the extensive wear of the substrate (Mg) and the presence of wear particles between the mating surfaces of the composite and the pin during the wear test [39]. The high level of fluctuations in Fig. 22a is thus attributed to the prominent particle agglomeration and insufficient particle dispersion in the Mg matrix. The mean friction coefficient declined from 0.47 to 0.31 and 0.19 in the 1000 and 1200-rpm-processed composites respectively. The fine and properly dispersed ZrO_2+CeO_2 particles are responsible for the lowered friction coefficient owing to their capacity to act as hard obstacles required for loadbearing and wear resistance. The fine ZrO_2+CeO_2 particles are adjudged to have offered substantial resistance against sliding or improved abrasive wear during the wear test. This outcome lowers the wear loss, and wear rate leading to a lowered friction coefficient. The formation of a stable tribo-layer is also another factor aiding a lesser friction coefficient in the composite. The CeO_2 particles provided the solid lubrication effect in the FSP'ed Al5083/SiC/CeO_2 composite to significantly improve the friction coefficient and wear resistance of the composite [28].

3.5. *Corrosion behaviour*

The open circuit potentials (OCP) and corrosion potential vs. current density curves of the AZ31B Mg/ZrO_2+CeO_2 hybrid composite are shown in Fig. 23a and b respectively. The OCP vs. time of the AZ31B Mg/ZrO_2+CeO_2 hybrid composites revealed that the higher tool's rotating speed produced higher OCP. The highest OCP is thus obtained with the 1200 rpm-FSP

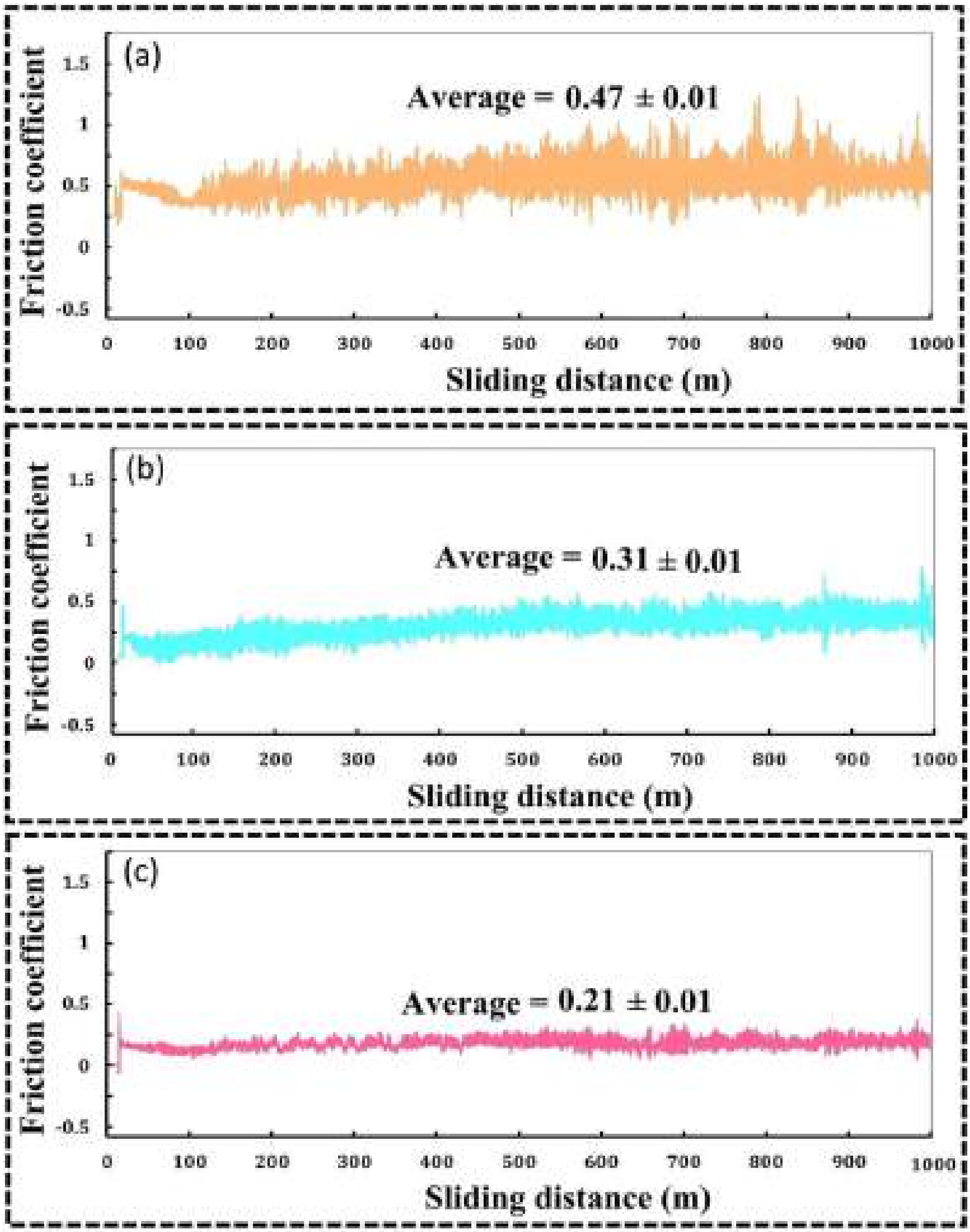

Fig. 22 – Friction coefficient vs. sliding distance results of the AZ31B Mg/ZrO_2+CeO_2 hybrid composite processed at (a) 800, (b) 1000, and (c) 1200 rpm.

processed composite. The extrapolated corrosion potentials and current densities from the curves are revealed in Table 5. The corrosion potentials of -1.91 ± 0.02 V, -1.83 ± 0.02 V, and -1.71 ± 0.02 V were obtained from the 800, 1000, and 1200 rpm-composite samples respectively while their corresponding current densities were 5.118×10^{-3} A/cm^2, 4.729×10^{-3} A/cm^2, and 3.217×10^{-3} A/cm^2 respectively. From these results, the corrosion potential increases with the rotating speed of the tool while there is a decline in the current density. This shows that an improvement in corrosion resistance and a decrease in corrosion rate ensue in the FSP's AZ31B Mg/ZrO_2+CeO_2 hybrid composites as the rotating speed of the tool was increased. The desirable corrosion resistance is thus attained in the 1200 rpm-FSP processed

Table 4 – Wear rate of the AZ31B Mg/ZrO_2+CeO_2 hybrid composite.

Sample	Wear rate (mm^3/Nm)
800 rpm	4.09×10^{-5}
1000 rpm	3.56×10^{-5}
1200 rpm	2.87×10^{-5}

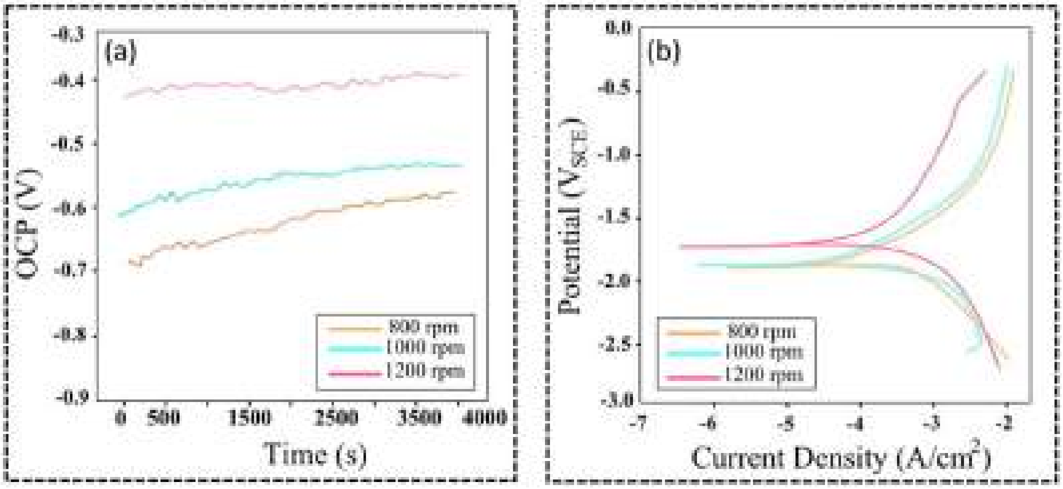

Fig. 23 – Corrosion results of the AZ31B Mg/ZrO_2+CeO_2 hybrid composite (a) OCP, (b) corrosion potential vs. current density.

Table 5 – Extrapolated corrosion potential and current densities.

Samples produced at rpm	E_{corr} (V)	i_{corr} (A/cm^2)
800	−1.91 ± 0.02	5.118 ×10 $^{-3}$
1000	−1.83 ± 0.02	4.729 ×10 $^{-3}$
1200	- 1.71 ± 0.02	3.217 ×10 $^{-3}$

composite. The enhancement in the corrosion properties of the composite could be related to the inherent finely dispersed ZrO_2+CeO_2 particles in the 1200 rpm-FSP processed composite. Qianhao Zang et al. [1] reported that the increase in the volume fraction of the reinforcement (graphene nanoplatelets - GNPs) enhanced the corrosion behaviour of the AZ31/GNPs composite.

Fig. 24 shows the corroded surfaces of the AZ31B Mg/ZrO_2+CeO_2 hybrid composites developed with dissimilar rotating speeds of the FSP tool. Severe corrosion attack is observed in Fig. 24a (800 rpm) and Fig. 24b (1000 rpm) while the level of corrosion attack significantly declined in Fig. 24c (1200 rpm). It has been reported that the decrease in the interparticle distance cut back the level of corrosion attack in composites [49]. As a result, the composite sample with uneven distribution of ZrO_2+CeO_2 particles (or with particle agglomeration) suffered significant corrosion attack as observed in Fig. 24a and b. A direct relationship has been reported to exist between grain structure and corrosion resistance as the fine evenly dispersed equiaxed structure of the AZ31B alloy improved the corrosion attack of the alloy [50]. The substantial modification/refinement of the structure of the AZ31B Mg/ZrO_2+CeO_2 hybrid composite at 1200 rpm could be a major factor for the least corrosion attack in Fig. 24c. In another view, the presence of particle agglomeration, void, and tunnel defects could have aided the corrosion attack in Fig. 24a (800 rpm) more than in Fig. 24c. According to Zhang et al. [51], the presence of voids or micropores in the Al-reinforced composite accelerated corrosion attack/rate by facilitating the diffusion of Cl-in the matrix of the composite. The variation in the rotating speed of the tool is adjudged to have caused a disparity in the material flow, surface characteristics, and microstructural features of the AZ31B Mg/ZrO_2+CeO_2 hybrid composites. These changes could have

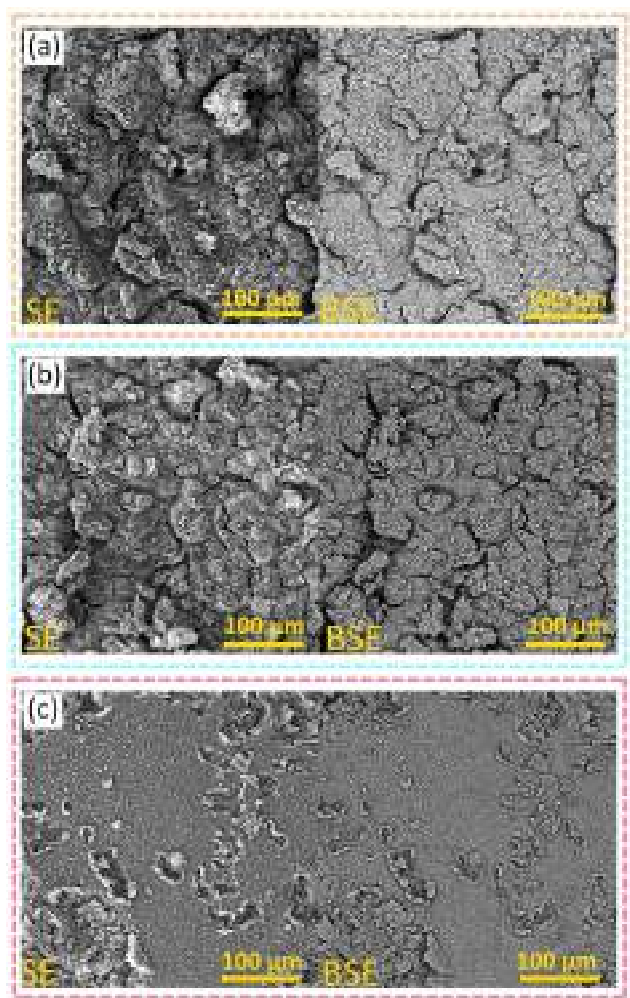

Fig. 24 – Corroded surfaces of the AZ31B Mg/ZrO_2+CeO_2 hybrid composite (a) 800, (b) 1000, and (c) 1200 rpm.

played an important role in the corrosion behaviour of the composites. It was revealed that the surface formation features of the CNT-reinforced AZ31 composite enhanced the corrosion resistance of the composite [49]. Corrosion resistance is attributed to the formation of an improved passive layer linked to the presence of uniformly dispersed fine particles [45]. The presence of rare-earth element CeO_2 particles in the AA7075/MoS_2/CeO_2 hybrid composite hindered the corrosion propagation in the studies of Maji et al. [52]. As a result, lesser sites of CeO_2 owing to particle agglomeration in the AZ31B Mg/ZrO_2+CeO_2 hybrid composite could thus be the reason for the rapid corrosion attack and propagation in Fig. 24a and b [53]. The metallurgical changes induced by the FSP process are considered to have augmented the corrosion rate and resistance of the AZ31B Mg/ZrO_2+CeO_2 hybrid composite at 1200 rpm without deteriorating the mechanical (shear and tensile) properties of the composite.

4. Conclusions

The hybridized AZ31B Mg/ZrO_2+CeO_2 composites were successfully developed through the friction stir processing method under a variable tool rotational speed setting. The macro- and micro-structure, hardness, shear punching properties, tensile strength, tribological properties (wear rate, weight/wear loss, friction coefficient, worn surfaces, and debris), and corrosion behaviours of the AZ31B Mg/ZrO_2+CeO_2 hybrid composites were studied in detail. The obtained findings are summarized as follows.

i. The level of the rotating speed of the FSP tool controls the ZrO_2+CeO_2 distribution and flow-related discontinuity of the AZ31B Mg/ZrO_2+CeO_2 hybrid composite.
ii. The mean ZrO_2+CeO_2 particle sizes of the composites were reduced (4.52 μm–2.49 μm) while the average grain sizes of the composites also lessened (7.39 μm–3.38 μm) as the tool's processing speed was elevated. These are due to the higher rotating tool-induced plastic straining, dynamic recrystallization, and particle-aided pinning phenomena.
iii. Microhardness of the AZ31B Mg/ZrO_2+CeO_2 hybrid composite increases from 99 to 135 HV as the speed was increased from low level (800 rpm) to 1200 rpm as a result of the grain refinement and the uniformly dispersed ZrO_2+CeO_2 particles in the composite.
iv. Sufficient material flow, better dispersion/refinement of the ZrO_2+CeO_2 particles, and elimination of defects improved the shear strength (121–237 MPa) of the AZ31B Mg/ZrO_2+CeO_2 hybrid composite after the elevation in the tool's speed.
v. The tensile strength of the AZ31B Mg/ZrO_2+CeO_2 hybrid composite increased from 172 to 228 MPa when there was a rise in the tool's speed due to defect elimination and particle-aided strengthening.
vi. The finer and evenly dispersed ZrO_2+CeO_2 particles and hardness improvement decreased the wear properties of the composite as the tool's rotating speed was increased.
vii. Corrosion enhancement was achieved in the AZ31B Mg/ZrO_2+CeO_2 hybrid composite after increasing the tool's rotating speed due to the inherent finer Mg grains and finely dispersed ZrO_2+CeO_2 particles in the composite.

Declaration of competing interest

The authors declare that they have no known competing financial interests or personal relationships that could have appeared to influence the work reported in this paper.

REFERENCES

[1] Zang Qianhao, Chen Hongmei, Zhang Jing, Wang Ling, Chen Shujin, Jin Yunxue. Microstructure, mechanical properties and corrosion resistance of AZ31/GNPs composites prepared by friction stir processing. J Mater Res Technol 2021;14:195–201.
[2] Chang CI, Wang YN, Pei HR, Lee CJ, Du XH, Huang JC. Microstructure and mechanical properties of nano-ZrO2 and nano-SiO_2 particulate reinforced AZ31-Mg based composites fabricated by friction stir processing. Key Eng Mater 2007;351:114–9.
[3] Bai Xingyu, Hu Conglin, Wei Guobing, Guo Li, Chen Hao, Li Bin. Good strength-plasticity compatibility of GNP/AZ31 composites fabricated by FSP: microstructural evolution and mechanical properties. J Mater Res Technol 2022;20:3995–4007.
[4] Behnamian Yashar, Serate Dominic, Aghaie Ermia, Zahiri Ramin, Tolentino Zachary, Hamid Niazi, Mostafaei Amir. Tribological behavior of ZK60 magnesium matrix composite reinforced by hybrid MWCNTs/B_4C prepared by stir casting method. Tribol Int 2022;165:107299.
[5] Muhammet Emre Turan, Sun Yavuz, Akgul Yasin. Mechanical, tribological and corrosion properties of fullerene reinforced magnesium matrix composites fabricated by semi-powder metallurgy. J Alloys Compd 2018;740:1149–58.
[6] Casas-Luna Mariano, Montufar Edgar B, Hort Norbert, Díaz-de-la-Torre Sebastian, Méndez-García José Claudio, Vištejnová Lucie, et al. Degradable magnesium-hydroxyapatite interpenetrating phase composites processed by current assisted metal infiltration in additive-manufactured porous preforms. J Magn Alloy 2022;10:3641–56.
[7] Yao Yantao, Chen Liqing. Processing of B_4C particulate-reinforced magnesium-matrix composites by metal-assisted melt infiltration technique. J Mater Sci Technol 2014;30:661–5.
[8] Srivastava Ashish Kumar, Amit Rai Dixit, Maurya Manish, Saxena Ambuj, , Nagendra Kumar Maurya, Prakash Dwivedi Shashi. Rajesh bajaj, 20th century uninterrupted growth in friction stir processing of lightweight composites and alloys. Mater Chem Phys 2021;266:124572.
[9] Qiao Ke, Zhang Ting, Wang Kuaishe, Yuan Shengnan, Wang Liqiang, Chen Shanyong, Wang Yuhao, Xue Kairui, Wang Wen. Effect of multi-pass friction stir processing on the microstructure evolution and corrosion behavior of

ZrO2/AZ31 magnesium matrix composite. J Mater Res Technol 2022;18:1166–79.

[10] Paidar Moslem, Bokov Dmitry, Mehrez Sadok, Ojo Olatunji Oladimeji, , Vaira Vignesh Ramalingam, Memon Shabbir. Improvement of mechanical and wear behavior by the development of a new tool for the friction stir processing of Mg/B_4C composite. Surf Coating Technol 2021;426:127797.

[11] Sharma Sanjay, Amit Handa, Singh Sahib Sartaj, Verma Deepak. Influence of tool rotation speeds on mechanical and morphological properties of friction stir processed nanohybrid composite of MWCNT-Graphene-AZ31 magnesium. Journal of Magnesium and Alloys 2019;7:487–500.

[12] Abbas Aqeel, Huang Song Jeng, Ballokova Beata, Sülleiova Katarína. Tribological effects of carbon nanotubes on magnesium alloy AZ31 and analyzing aging effects on CNTs/AZ31 composites fabricated by stir casting process. Tribol Int 2020;142:105982.

[13] Dinaharan Isaac, Zhang Shuai, Chen Gaoqiang, Shi Qingyu. Titanium particulate reinforced AZ31 magnesium matrix composites with improved ductility prepared using friction stir processing. Mater Sci Eng, A 2020;772:138793.

[14] Vedabouriswaran G, Aravindan S. Development and characterization studies on magnesium alloy (RZ 5) surface metal matrix composites through friction stir processing. Journal of Magnesium and Alloys 2018;6:145–63.

[15] Liu Fenjun, Yan Ji, Sun Zhiyong, Liu Jianbo, Bai Yanxia, Shen Zhikang. Enhancing corrosion resistance and mechanical properties of AZ31 magnesium alloy by friction stir processing with the same speed ratio. J Alloys Compd 2020;829:154452.

[16] Gültekin Deniz, Duru Erhan, Akbulut Hatem. Improved wear behaviors of lead-free electroless Ni–B and Ni-B/ CeO_2 composite coatings. Surf Coating Technol 2021;422:127525.

[17] Das Himadri Tanaya, Balaji Elango, Dutta Swapnamoy, Das Nigamananda, Das Payaswini, Mondal Aniruddha, Imran Muhammad. Recent trend of CeO2-based nanocomposites electrode in supercapacitor: a review on energy storage applications. J Energy Storage 2022;50:104643.

[18] Zhang Weiwei, Li Baosong, Hong Ming, Li Mingyuan. Effects of cerium oxide doping on microstructure and properties of Ni-GO-CeO_2 nanocomposite coatings. J Mater Res Technol 2022;21:3440–50.

[19] An Kai, Sui Yi, Qing Yongquan, Yang Chuanning, Cai Long, Wang Linshan, Liu Changsheng. Synergistic reinforcement coating with anti-corrosion and UV aging resistance by filling modified CeO_2 nanoflakes. Colloids Surf A Physicochem Eng Asp 2021;625:126904.

[20] Aydin Fatih, Durgut Rafet, Mustu Mustafa, Demir Bilge. Prediction of wear performance of ZK60/CeO_2 composites using machine learning models. Tribol Int 2023;177:107945.

[21] Mazaheri Yousef, Mahdi Jalilvand Mohammad, Heidarpour Akbar, Amir Reza Jahani. Tribological behavior of AZ31/ZrO_2 surface nanocomposites developed by friction stir processing. Tribol Int 2020;143:106062.

[22] Navazani Mohammad, Dehghani Kamran. Fabrication of Mg-ZrO2 surface layer composites by friction stir processing. J Mater Process Technol 2016;229:439–49.

[23] Sathish T, Muthu G, Vijayakumar MD, Dhinakaran V, Bupathi Ram PM. Mechanical properties and microstructural analysis of friction stir processed AA6056-zirconium dioxide (ZrO_2). Mater Today Proc 2021;37:1804–8.

[24] Veeresh Kumar GB, Pramod R, Sekhar Ch Guna, Pradeep Kumar G, Bhanumurthy T. Investigation of physical, mechanical and tribological properties of Al6061–ZrO2 nano-composites. Heliyon 2019;5:e02858.

[25] Shu Da, Dai Sichao, Wang Gang, Si Wudong, Xiao Ping, Cui Xiangxiang, Chen Xu. Influence of CeO_2 content on WC morphology and mechanical properties of WC/Ni matrix composites coating prepared by laser in-situ synthesis method. J Mater Res Technol 2020;9:11111–20.

[26] Luo Jie, Liu Shoufa, Paidar Moslem, Vaira Vignesh R, Mehrez Sadok. Enhanced mechanical and tribological properties of AA6061/CeO2 composite fabricated by friction stir processing. Mater Lett 2022;318:132210.

[27] Karthik A, Srinivasan SA, Karunanithi R, Kumaresh Babu SP, Jain Vikram Kumar S. Influence of CeO_2 reinforcement on microstructure, mechanical and wear behavior of AA2219 squeeze cast composites. J Mater Res Technol 2021;14:797–807.

[28] Amra M, Ranjbar Khalil, Hosseini SA. Microstructure and wear performance of Al5083/CeO_2/SiC mono and hybrid surface composites fabricated by friction stir processing. Trans Nonferrous Metals Soc China 2018;28:866–78.

[29] Mahdi Jalilvand Mohammad, Mazaheri Yousef. Effect of mono and hybrid ceramic reinforcement particles on the tribological behavior of the AZ31 matrix surface composites developed by friction stir processing. Ceram Int 2021;46:20345–56.

[30] Sharifitabar M, Kashefi M, Khorshahian S. Effect of friction stir processing pass sequence on properties of Mg–ZrSiO4–Al_2O_3 surface hybrid micro/nano-composites. Mater Des 2016;108:1–7.

[31] Liu Fen-jun, Yan Ji, Bai Yan-Xia. Influence of multipass high rotating speed friction stir processing on microstructure evolution, corrosion behavior and mechanical properties of stirred zone on AZ31 alloy. Trans Nonferrous Metals Soc China 2020;30:3263–73.

[32] Tong Lian, Xie Jianing, Liu Li, Gong Chang, Ojo Olatunji Oladimeji. Microscopic appraisal and mechanical behavior of hybrid Cu/Al joints fabricated via friction stir spot welding-brazing and modified friction stir clinching-brazing. J Mater Res Technol 2020;9:13239–49.

[33] Heydari Farhood, Ahmad Ali Amadeh, Ojo Olatunji Oladimeji, Hossein Hasanniya Mohammad, Tamizifar Mortaza. Microstructure and mechanical properties of autobody steel joined by friction stir spot welding. Sādhanā 2019;44.

[34] Shen Jun, Dong Min, Wang Dan. Effects of heating process on the microstructures and tensile properties of friction stir spot welded AZ31 magnesium alloy plates. Mater Des 2011;32:5033–7.

[35] Harwani Deepika, Badheka Vishvesh, Patel Vivek. High-temperature tensile deformation in single-pass friction stirred AZ31 alloy. International Journal of Lightweight Materials and Manufacture 2023;6:140–8.

[36] Dinaharan Isaac, Zhang Shuai, Chen Gaoqiang, Shi Qingyu. Assessment of Ti-6Al-4V particles as a reinforcement for AZ31 magnesium alloy-based composites to boost ductility incorporated through friction stir processing. Journal of Magnesium and Alloys 2022;10:979–92.

[37] Liu Fenjun, Yapeng Zhiyong Sun, Yan Ji. Corrosion resistance and tribological behavior of particles reinforced AZ31 magnesium matrix composites developed by friction stir processing. J Mater Res Technol 2021;11:1019–30.

[38] Paidar Moslem, Ojo Olatunji Oladimeji, Ezatpour Hamid Reza, Akbar Heidarzadeh. Influence of multi-pass FSP on the microstructure, mechanical properties and tribological characterization of Al/B4C composite fabricated by accumulative roll bonding (ARB). Surf Coating Technol 2019;361:159–69.

[39] Ali Moharrami, Ahmad Razaghian, Paidar Moslem, Slapakova Michaela, Ojo Olatunji Oladimeji, Taghiabadi Reza. Enhancing the mechanical and tribological

properties of Mg2Si-rich aluminum alloys by multi-pass friction stir processing. Mater Chem Phys 2020;250:123066.

[40] Fernanda Rocha Chiuzuli, Bruna Fernanda Batistao, Luciano Andrei Bergmann, Nelson Guedes de Alcantara, Jorge Fernandez dos Santos, Klusemann Benjamin, Gargarella Piter. Effect of the gap width in AZ31 magnesium alloy joints obtained by friction stir welding. J Mater Res Technol 2021;15:5297–306.

[41] Meng Xiangchen, Huang* Yongxian, Cao Jian, Shen Junjun, Jorge F, dos Santos. Recent progress on control strategies for inherent issues in friction stir welding. Prog Mater Sci 2021;115:100706.

[42] Patel M, Chaudhary B, Murugesan J, Jain NK, Patel V. Enhancement of tensile and fatigue properties of hybrid aluminum matrix composite via multipass friction stir processing. J Mater Res Technol 2022. https://doi.org/10.1016/j.jmrt.2022.11.073.

[43] Liu Shoufa, Zhang Shaoguo, Vaira Vignesh R, Ojo Olatunji Oladimeji, Mehrez Sadok, Mohanavel Vinayagam, Paidar Moslem. Probe-less friction stir spot processing (PFSSP) of AA5754/AA5083 joint by adding the B_4C ceramics: effect of shoulder features on mechanical properties and tribological behavior. Vacuum 2023;207:111542.

[44] Liu Shoufa, Paidar Moslem, Mehrez Sadok, Ojo Olatunji Oladimeji, Mahariq Ibrahim, Elbadawy Ibrahim. Development of AA6061/316 stainless steel surface composites via friction stir processing: effect of tool rotational speed. Mater Char 2022;192:112215.

[45] Liu Shoufa, Paidar Moslem, Mehrez Sadok, Ojo Olatunji Oladimeji, Omar Cooke Kavian, Wang Yinwei. Fabrication of AA6061/316 composites via a double pin FSP tool. J Mater Res Technol 2022;20:2826–40.

[46] Dinaharan I, Zhang S, Chen G, Shi Q. Development of titanium particulate reinforced AZ31 magnesium matrix composites via friction stir processing. J Alloys Compd 2020;820:153071.

[47] Paidar Moslem, Sarab Mahsa Laali. Friction stir spot welding of 2024-T3 aluminum alloy with SiC nanoparticles. J Mech Sci Technol 2016;30:365–70.

[48] Paidar Moslem, Ali Asgari, Ojo Olatunji Oladimeji, Saberi Abbas. Mechanical properties and wear behavior of AA5182/WC nanocomposite fabricated by friction stir welding at different tool traverse speeds. J Mater Eng Perform 2018;27:1714–24.

[49] Liu F, Li A, Shen Z, Chen H, Ji Y. Microstructure and corrosion behavior of Al-Ti-TiC-CNTs/AZ31 magnesium matrix composites prepared using laser cladding and high-speed friction stir processing. Opt Laser Technol 2022;152:108078.

[50] Patel V, Li W, Andersson J, Li N. Enhancing grain refinement and corrosion behavior in AZ31B magnesium alloy via stationary shoulder friction stir processing. J Mater Res Technol 2022;17:3150–6.

[51] Zhang Mingming, Paidar Moslem, Ojo Olatunji Oladimeji, Mehrez Sadok, Narayanasamy Stalin, Mohd Zain Azlan, Mohanavel Vinayagam. Impact of multiple FSP passes on structure, mechanical, tribological and corrosion behaviors of AA6061/316 stainless-steel reinforced Al matrix composites. Surf Coating Technol 2022;447:128801.

[52] Maji Pabitra, Nath Rahul Kanti, Pritam Paul RK. Bhogendro Meitei, Subrata Kumar Ghosh, Effect of processing speed on wear and corrosion behavior of novel MoS2 and CeO_2 reinforced hybrid aluminum matrix composites fabricated by friction stir processing. J Manuf Process 2021;69:1–11.

[53] Xie Yuming, Meng Xiangchen, Chang Yuexin, Mao Dongxin, Qin Zhiwei, Wan Long, Huang Yongxian. Heteroatom modification enhances corrosion durability in high-mechanical-performance graphene-reinforced aluminum matrix composites. Adv Sci 2022:2104464.